

1 **In-depth study of the formation processes of single atmospheric particles in**

设置格式[Li]: 字体颜色: 自动设置

2 **the southeastern margin of Tibetan Plateau**

3 Li Li^{1,3}, Qiyuan Wang^{1,2}, Jie Tian¹, Huikun Liu¹, Yong Zhang¹, Steven Sai Hang Ho⁴,
4 Weikang Ran¹, Junji Cao⁵

5 ¹ Key Laboratory of Aerosol Chemistry and Physics, State Key Laboratory of Loess and Quaternary
6 Geology, Institute of Earth Environment, Chinese Academy of Sciences, Xi'an 710061, China

7 ² CAS Center for Excellence in Quaternary Science and Global Change, Xi'an 710061, China

8 ³ University of Chinese Academy of Sciences, Beijing 100049, China

9 ⁴ Division of Atmospheric Sciences, Desert Research Institute, Reno, NV 89512, United States

10 ⁵ Institute of Atmospheric Physics, Chinese Academy of Sciences, Beijing 100029, China

11
12 Correspondence to: Qiyuan Wang (wangqy@ieecas.cn) and Junji Cao (jjcao@mail.iap.ac.cn).

13

14 **Abstract**

15 The unique geographical location of the Tibetan Plateau (TP) plays an important role in
16 regulating global climate change, but the impacts of the chemical components and
17 atmospheric processing on the size distribution and mixing state of individual particles are
18 rarely explored in the southeastern margin of the TP, which is a transport channel for
19 pollutants from Southeast Asia [to the TP](#) during the pre-monsoon season. Thus a
20 single-particle aerosol mass spectrometer (SPAMS) was deployed to investigate how the local
21 emissions of chemical composition interact with the transporting particles and assess the
22 mixing state of different particle types and secondary formation in this study. The TP particles
23 were classified into six main types: the rich-potassium (rich-K) type was the largest fraction
24 of the total particles (30.9%), followed by the biomass burning (BB) type (18.7%). Most
25 particle types were mainly transported from the surroundings [of the sampling site](#) and
26 [Sino-Myanmar border](#); but the air masses from northeastern India and Myanmar show a
27 greater impact on the number fraction of BB (31.7%) and Dust (18.2%) types, respectively.
28 [Then](#), the two episodes, with high particle concentrations showed that the differences in the
29 meteorological conditions in the same [trajectory](#) clusters could cause significant changes in
30 chemical components, especially the Dust and EC-aged types, [which](#) changed by a sum of
31 93.6% and 72.0%, respectively. Ammonium and Dust particles distribute at a relatively larger
32 size (~ 600 nm), but the size peak of other types is present at ~ 440 nm. [Compared with the](#)
33 [abundant sulfate \(⁹⁷HSO₄⁻\), the low nitrate \(⁶²NO₃⁻\) internally mixed in TP particles is mainly](#)
34 [due to the fact that nitrate is more volatilized](#), during the transport process. [The formation](#)
35 [mechanism of secondary speciation demonstrate that the formation capacity of atmospheric](#)
36 [oxidation is presumably affected by the convective transmission and the regional transport in](#)
37 [TP. However, the relative humidity \(RH\) could significantly promote the formation of](#)
38 [secondary species, especially ⁹⁷HSO₄⁻ and ¹⁸NH₄⁺](#). This study provides insights that can
39 improve the knowledge of particle composition and size, mixing state, and aging mechanism
40 at high time resolution over the TP region.

41 **Keywords**

42 Southeastern Tibetan Plateau, Individual particles, Chemical characteristics, [mixing state](#),
43 [Secondary formation](#)

删除[Li]: cross-border of northern Myanmar

删除[Li]: Besides

删除[Li]: events

删除[Li]: air

删除[Online_Group]: easily

删除[Li]: The easily volatilized nitrate (⁶²NO₃⁻)

删除[Li]: leads the more abundant sulfate (⁹⁷HSO₄⁻) to r

删除[Online_Group]: results of the

删除[Li]: secondary

设置格式[Li]: 字体: (默认) Times New Roman, 小四

删除[Online_Group]: species

设置格式[Li]: 字体颜色: 自动设置

删除[Online_Group]: is

设置格式[Li]: 字体: (默认) Times New Roman, 小四

设置格式[Li]: 字体颜色: 自动设置

删除[Online_Group]: weakene

设置格式[Li]: 字体: (默认) Times New Roman, 小四

设置格式[Li]: 字体颜色: 自动设置

删除[Li]: strengthen by

设置格式[Li]: 字体: (默认) Times New Roman, 小四

删除[Li]: regioinal

设置格式[Li]: 字体颜色: 自动设置

删除[Online_Group]: affected by the PBL height,

删除[Online_Group]: but

删除[Li]: C₂H₃O⁺, HC₂O₄⁻, NH₄⁺, NO₃⁻, and HSO₄⁻, seve

删除[Li]: The mechanism of secondary speciation sugges

设置格式[Li]: 字体: (默认) Times New Roman, 小四

设置格式[Li]: 字体颜色: 自动设置

删除[Li]: Pre-monsoon,

删除[Li]: Atmospheric

删除[Li]: aging,

44 1 Introduction

45 Atmospheric aerosols have complex components and sources and can be coated with
46 inorganic or organic materials during transport and atmospheric processing (Crippa et al.,
47 2013). After further coating through coagulation, condensation, and photochemical oxidation,
48 its sizes, chemical compositions, mixing states, and optical properties would change greatly,
49 leading to its influence in the atmosphere more uncertain (Jacobson, 2002; Zaveri et al., 2010;
50 Matsui, 2016; Budisulistiorini et al., 2017; Ma et al., 2012). Currently, the influences of the
51 complex chemical components on aerosol size and mixing state show large regional
52 differences due to the variations in the pollution sources, atmospheric formation mechanism
53 and meteorological conditions, which have been widely studied in an urban area at a low
54 altitude (Pratt et al., 2011; Liu et al., 2020a; Xu et al., 2017; Wang et al., 2022). However,
55 previous study found that the migration or formation of low-volatile component (such as
56 nitrate and organic matter) could effectively be reduced due to evaporation during the upward
57 transportation process (Liu et al., 2020b), which further alter the chemical compositions and
58 the particle sizes. The transportation of the aerosols to a relatively cleaner environment
59 prevails the formation of secondary chemicals at a high altitude (Liu et al., 2020b). Therefore,
60 a comprehensive investigation of the detailed characteristic of aerosol formation and mixing
61 states is required to understand their environmental effects in low-, and high-altitude.

62 As a typical high-altitude region, the Tibetan Plateau (TP) has the highest and largest
63 mountain area in the world, which is the most sensitive and obvious indicator of climate
64 change in the entire Asian continent (Liu et al., 2017; Chen and Bordonni, 2014; Immerzeel et
65 al., 2010). In recent decades, many studies have shown that the melting and retreat of glaciers
66 in the TP regions is accelerating, and the main reason is attributable to anthropogenic
67 emissions, such as greenhouse gases and aerosols (Luo et al., 2020; Hua et al., 2019).
68 Atmospheric aerosols also can act as cloud condensation nuclei to impact the local
69 hydrological cycles and monsoon patterns by changing the microphysical properties and life
70 span of clouds (Qian et al., 2011; Gettelman et al., 2013; Kumar et al., 2017). The southern
71 part of the TP is always affected by the transport of more polluted air from South Asia along
72 the mountain valleys, especially during the pre-monsoon (i.e., March-May) with the

删除[Li]: When

删除[Li]: ed

删除[Li]: ,

删除[Li]: their

删除[Li]: physical and chemical properties

删除[Online_Group]: will

删除[Online_Group]: making

删除[Li]: their impact

删除[Li]: on the air

删除[Online_Group]: has

删除[Online_Group]: of

删除[Li]: The ability of aerosol particles to affect atmospheric conditions is dependent on their sizes, chemical compositions, and mixing states (Mc Figgans et al., 2006; Dusek et al., 2006)

删除[Li]: For example, dust aerosol is an important factor affecting climate change through the interactions of various physical processes such as the direct radiative effect (Ding et al., 2012)

删除[Li]: However, the ability of secondary formation has regional differences due to the variations in precursors, source strengths, and meteorological conditions (Pratt et al., 2011)

删除[Li]: In addition, t

删除[Li]:

删除[Li]: Yao, et al., 2012;

删除[Li]: William et al., 2010;

删除[Li]: influence

删除[Li]: properties and life span of clouds as cloud condensation nuclei, and affect

删除[Li]: Seinfeld and Pandis, 2012, Xia et al., 2007;

73 southwest prevailing wind (Chan et al., 2017; Zhao et al., 2017; Han et al., 2020). Most
74 studies have focused on the optical characteristics within the TP; however, only a few
75 research has been conducted on aerosol components.

76 Present aerosol components studies conducted in TP mostly focus on exploring the
77 influence of light-absorbing carbon aerosols and dust particles on climate change by optical
78 or offline sampling methods (e.g., Wang et al., 2019a; Liu et al., 2021). There is a lack of
79 studies on the chemical composition, mixing states, and formation mechanism of aerosols in
80 the southeast margin and even the entire TP, especially using high-time resolved
81 measurements. Although time-integrated sampling with filter collection followed by
82 laboratory analyses has been widely adopted for the chemical characterization of aerosols (Li
83 et al., 2022a; Shen et al., 2015; Zhang et al., 2013). Drawbacks of the traditional approach
84 include low time resolution, high detection limit, and time- and labor-intensive procedures.
85 More advanced aerosol online measurement equipment with high-time resolution, such as the
86 aerosol chemical speciation monitor (ACSM) and aerosol mass spectrometer (AMS) (Ng et
87 al., 2011; Canagaratna et al., 2007) are mainly used to achieve online observation datasets of
88 non-refractory submicron aerosol (including the mass concentration of sulfate, nitrate,
89 ammonium, chloride, and organic; and their corresponding mass spectral). This is beneficial
90 to recognize the dynamic processes of source emission in the atmosphere (Du et al., 2015;
91 Zhang et al., 2019a). At the same time, aerosol time-of-flight mass spectrometry (ATOFMS)
92 (Dall'Osto et al., 2014), and single particle aerosol mass spectrometer (SPAMS) (Zhang et al.,
93 2020), are popular for characterizing atmospheric individual particles. These devices can
94 determine the chemical composition and size distribution of the particles in detail, such as the
95 dynamic processes of chemical aging, mixing state, and transport of the aerosols (Liang et al.,
96 2022; Li et al., 2022b; Zhang et al., 2019b). To the best knowledge, the advanced
97 measurement device has not yet been applied for the studies conducted in TP, leading to a
98 lack of in-depth research on the PM_{2.5} pollution in TP, especially in the southeastern margin,
99 which hinders our understanding of the distribution characteristics and formation mechanism
100 of aerosol components in high-altitude regions.

101 The southeastern margin of the TP is an important transitional zone between the
102 high-altitude TP and the low-altitude Yungui Plateau (Wang et al., 2019a; Zhao et al., 2017),

删除[Li]: Cao et al., 2010;

删除[Li]: Zhu et al., 2017;

删除[Li]: influence of

删除[Li]: properties

删除[Li]: a

删除[Li]: studies

删除[Li]: ve

删除[Li]: within the plateau

删除[Li]: full

删除[Li]: Chen et al., 2015;

删除[Online_Group]: -

设置格式[Li]: 字体: (默认) Times New Roman, 小四

删除[Li]: devices

设置格式[Li]: 字体颜色: 自动设置

删除[Li]: a

删除[Li]:

删除[Li]: emporal

删除[Li]: show the inability to measure the mixing state c

删除[Online_Group]: provide

删除[Li]: with high temporal resolution

删除[Online_Group]: ,

删除[Online_Group]: which

删除[Online_Group]: obtain

设置格式[Li]: 字体: (默认) Times New Roman, 小四

设置格式[Li]: 字体颜色: 自动设置

设置格式[Li]: 字体: (默认) Times New Roman, 小四

删除[Li]: Prather

设置格式[Li]: 字体颜色: 自动设置

删除[Li]: 199

删除[Li]: Li

删除[Li]: 11

删除[Li]: ould

删除[Li]: full

删除[Online_Group]: their

103 an ideal place for investigating the impacts of pollutants transport and formation in the
104 high-altitude zone. In this study, [continuous](#) field observation of individual particles (SPAMS)
105 was deployed on the southeastern margin of the TP during the pre-monsoon [period](#), to (i)
106 investigate the changes of chemical characteristics between transport and local fine particles
107 during pre-monsoon, (ii) determine the particle size distributions, and the mixing states of
108 different particle types, and (iii) assess the contributions of photooxidation and aqueous
109 reaction to the formation of the secondary species. These results would expand our
110 understanding of the chemical components, size distribution, mixing state, and aging
111 pathways of aerosols in the high-altitude areas in the TP and surrounding areas.

删除[Li]: a

删除[Li]: high-time resolution

删除[Li]: continuously

112 2 Methodology

113 2.1 [Sampling site](#)

删除[Li]: **Observation**

114 Intensive 1-month field observation was deployed at the rooftop (~ 10 m above [ground](#)
115 [level](#)) of the Lijiang Astronomical Station, Chinese Academy of Sciences (3260 m above sea
116 level; 26°41'24"N, 100°10'48"E), Gaomeigu County, Yunnan Province, China, during the
117 pre-monsoon period (from April 14th to May 13th, 2018). The nearest residential area is the
118 Gaomeigu village (3–5 km away) with a small population size of 113 residents in 27
119 households. [Villagers](#) [earn](#) a living by farming (e.g., potato and autumn rape), and biomass is
120 the [major domestic](#) fuel (Li et al., 2016). The site is surrounded by rural and mountainous
121 areas and has no obvious industry or traffic emissions. During the observation period, the
122 average temperature (T) and relative humidity (RH) are $8.4 \pm 3.1^{\circ}\text{C}$ and $69\% \pm 21\%$,
123 respectively. The wind speed (WS) is $2.2 \pm 1.2 \text{ m}\cdot\text{s}^{-1}$ with the prevailing wind in the north and
124 northeastern (Fig. S1).

删除[Li]: the

删除[Li]: . The villagers

删除[Li]: make

删除[Li]: main

删除[Li]: residential

125 2.2 On-line instrument

126 A detailed operational principle and the calibrations of the single-particle aerosol mass
127 spectrometer (SPAMS, Hexin Analytical Instrument Co., Ltd., Guangzhou, China) has been
128 described elsewhere (Li et al., 2011). Briefly, individual particles are drawn into SPAMS
129 through a critical orifice. The particles are focused and accelerated, then aerodynamically
130 sized by two continuous diode Nd: YAG laser beams (532 nm), subsequently desorbed and

131 ionized by a pulsed laser (266 nm) triggered exactly based on the velocity of the specific
132 particle. The generated of positive and negative molecular fragments are recorded with the
133 corresponding size of individual particles. In summary, a velocity, a detection [time](#), and an
134 ion mass spectrum are recorded for each ionized particle, while there is no mass spectrum for
135 not ionized particles. The velocity could be converted to d_{va} based on a calibration using
136 polystyrene latex spheres (PSL, Thermo Scientific Corp., Palo Alto, USA) with predefined
137 sizes. The average ambient pressure is 690 hPa (in a range of 685–694 hPa) during the
138 measurements and calibration. Particles measured by SPAMS mostly are within the size
139 range of vacuum aerodynamic diameter (d_{va}) 0.2–2.0 μm . [A hollow silicone dryer was
140 installed in front of the inlet. This reduces the uncertainty of particle collection efficiency due
141 to the changes of humidity in sampled airs.](#)

142 Meteorological parameters, including the planetary boundary layer (PBL), temperature
143 ($^{\circ}\text{C}$), RH (%), WS ($\text{m}\cdot\text{s}^{-1}$), and wind direction (WD) were continuously achieved using an
144 automatic weather station (Model MAWS201, Vaisala HydroMet, Helsinki, Finland) at a time
145 resolution of 5 min. Gaseous concentrations (ppbv) were obtained using a multiple gas
146 analyzer (Thermo Scientific Corp.), including ozone (O_3 , model 49i) and nitrogen oxides
147 (NO_x , model 42i) in a 5-min resolution. The SPAMS and gas analyzers are co-located in the
148 same position, while the weather station was uncovered outside ~ 5 m from the sampling
149 house. Time series of SPAMS particles, gaseous concentrations (NO , NO_x , O_3 , and CO) and
150 meteorological parameters (PBL, temperature, RH, WD, and WS) were shown in Fig. S2.

151 2.3 Individual particle classification

152 During the observation period, a total of 461,876 ambient particles with the size (d_{va}) of
153 0.2–2.0 μm were collected, including 55,583 in Episode I (E1; from April 18th 08:00 [local
154 time \(LT\)](#) to April 19th 08:00 [LT](#)) and 62,110 in Episode II (E2; from April 26th 17:00 [LT](#) to
155 April 28th 02:00 [LT](#)). The analyzed particles are classified into 1,557 [groups](#) using an adaptive
156 resonance theory neural network (ART-2a) with a vigilance factor of 0.8, a learning rate of
157 0.05, and 20 iterations (Song et al., 1999). Finally, eight major particle clusters [i.e.,
158 [potassium-rich \(rich-K\)](#), [biomass burning \(BB\)](#), [organic carbon \(OC\)](#), Ammonium, [aged
159 element carbon \(EC-aged\)](#), Dust, [sodium \(Na\)-potassium \(K\)-containing \(NaK-SN\)](#), and [iron](#)

删除[Li]: moment

设置格式[Li]: 字体: (默认) Times New Roman, 小四, 字体颜色: 自动设置

设置格式[Li]: 字体颜色: 自动设置

设置格式[Li]: 字体: (默认) Times New Roman, 小四, 字体颜色: 自动设置

设置格式[Li]: 字体颜色: 自动设置

删除[Li]: cluster

删除[Li]: P

删除[Li]: B

删除[Li]: B

删除[Li]: O

删除[Li]: C

删除[Li]: A

删除[Li]: ing

删除[Li]: E

删除[Li]: C

删除[Li]: S

删除[Li]: ,

删除[Li]: P

删除[Li]: I

(Fe)-lead (Pb)-containing (Metal)] with distinct chemical patterns were manually combined, which represent ~99.7 % of the population of the detected particles. The remaining particles are grouped as “Other”. The characteristics of the positive and negative mass spectra (MS) of each particle type are shown in Fig. S3. A detailed description of classification criteria for individual particles and the characteristic ion fragments for each particle type can be found in Text S1. [The criteria used for searching the some secondary species in the SPAMS datasets are summarized in Table S2.](#)

删除[Li]: L

2.4 Trajectory-related analysis

To determine the influence of regional transport on different particles at Gaomeigu, the trajectory clusters analysis was carried out using the 72-h backward air mass trajectories at [arrival heights of 500 m above ground level](#). The trajectories were calculated with the Hybrid Single-Particle Lagrangian Integrated Trajectory model (Draxler and Hess, 1998), and the meteorological data were obtained from the Global Data Assimilation System (GDAS; <ftp://arlftp.arlhq.noaa.gov/pub/archives/gdas1>, last access: 6 April, 2022). The cluster analysis employs a Euclidean-oriented distance definition to differentiate and cluster the major spatial features of the inputting trajectories. Details of the trajectory clustering method can be found in Sirois and Bottenheim (1995). To investigate the effects of transport on the chemical characteristic of the individual particles, trajectories with particle number concentrations high than the 75th percentile are considered as pollution (Liu et al., 2021).

删除[Li]: the

3 Results and Discussion

3.1 Characteristics of particle composition

Table 1 summarizes the numbers of concentrations, relative percentages, and characteristic ions of each particle type. The most dominant particle type in Gaomeigu during pre-monsoon is rich-K, accounting for an average of 30.9% of the total resolved particles, followed by BB (18.7%), OC (12.8%), Ammonium (11.9%), EC-aged (10.9%), and Dust (10.7%). Similar to the results of some studies in urban areas, rich-K or carbonaceous-containing type is the dominant particle type (15-50%) ([Xu et al., 2018; Wang et al., 2019b; Li et al., 2022](#)). [The difference is that](#) few researchers can capture the high

删除[Li]: Li et al., 2014; Zhang et al., 2015; Shen et al., 2017; Zhang et al., 2017;

删除[Li]: Differently,

188 proportion of Ammonium particles as shown in this study (Shen et al., 2017; Xu et al., 2018),
189 which is ascribed to the conversion of ammonia (NH₃) precursor emitted from large-scale
190 agricultural activities and mountain forest (Engling et al., 2011; Li et al., 2013). It is
191 necessary to point out that 60% of Ammonium particles contain signals of [amine fragment](#)
192 (m/z 58, C₂H₅NH=CH₂⁺), implying their similar formation pathway (Zhang et al., 2012).
193 Moreover, the [amine](#)-containing particle represented 12.5% of the total ambient particles,
194 which is significantly higher than that in some urban areas at low altitudes (around 2%) (Cahi
195 et al., 2012; Zhang et al., 2015; Li et al., 2017) but is comparable to [that at observed sites](#)
196 [with](#), high RH, [or during](#) fog and cloud events at a high altitude (> 9%) (Roth et al., 2016; Lin
197 et al., 2019). This suggests that the formation of amines under high RH and fog conditions
198 might exist in the Gaomeigu area (with an altitude of 3260 m), for example, the high relative
199 fraction of [amine](#)-containing particle corresponds to a high RH (Fig. S4), and the existence of
200 amine sources govern the ammonium formations (Bi et al., 2016; Rehbein et al., 2011). The
201 relatively larger fraction of Dust particles is related to the short-time occurrences of dust
202 events in spring (Fig. S5), leading to a wide contribution ranging between 10% and 70% in
203 the period of 19:00 [LT](#) on April 16th to 10:00 [LT](#) on April 17th.

204 Fig. 1 shows the diurnal variations of each particle type. The rich-K, BB, and OC
205 particles decrease after midnight until 06:00 [LT](#), possibly explained by the curtailment of
206 local traffic and biomass-burning activities [at nighttime](#) even though both the planetary
207 boundary layer (PBL) height and WS decrease (Fig. S6). Then, [their intensities](#) rapidly
208 increase [in the morning \(around 07:00 LT\)](#), [due to more](#) pollutants from biomass burning [and](#)
209 [traffic emissions](#), [at](#) the upwind region. [The increases of PBL height and WS also lead to the](#)
210 [air pollutants transported from the surrounding environment to the sampling site](#) (Liu et al.,
211 2021). At 11:00 [LT](#), the particle counts sharply decrease till 16:00–17:00 [LT](#), caused by the
212 pollutant dispersion with the increases of the PBL height and WS. Increasing trends are
213 observed after 17:00 [LT](#) due to the reduction of PBL height and WS. In contrast, the
214 Ammonium, EC-aged, and Dust particles show a unimodal pattern of the daily diurnal
215 variation (Fig. 1d–f). From 00:00 to 06:00 [LT](#), minor fluctuation of particle concentrations of
216 Ammonium, EC-aged, and Dust is observed for these particle types. [After that, their levels](#)
217 continuously elevate until [~11:00 LT](#) due to [the regional transport, traffic emission, and](#)

删除[Li]: diethylamine

删除[Li]: DEA,

删除[Li]: ⁵⁸

删除[Li]: DEA

删除[Li]: Pratt and Prather, 2010;

删除[Online_Group]: the

删除[Online_Group]: in processing of

删除[Li]: DEA

删除[Li]: ; Zhang et al., 2012

删除[Online_Group]: y

删除[Li]: around 07:00

删除[Online_Group]: when the

删除[Online_Group]: are transported from

删除[Online_Group]: as t

删除[Online_Group]: rising

删除[Online_Group]: the

删除[Li]: rises

删除[Online_Group]: due

删除[Online_Group]: intensive distribution of biomass

设置格式[Li]: 字体颜色: 自动设置, 非突出显示

删除[Online_Group]: y

设置格式[Li]: 字体颜色: 自动设置

设置格式[Li]: 字体颜色: 自动设置, 非突出显示

设置格式[Li]: 字体颜色: 自动设置

删除[Online_Group]: about

设置格式[Li]: 字体颜色: 自动设置, 非突出显示

删除[Li]: 2

设置格式[Li]: 字体: 非倾斜, 字体颜色: 自动设置

设置格式[Li]: 字体颜色: 自动设置, 非突出显示

删除[Online_Group]: increased of anthropogenic emissio

设置格式[Li]: 字体颜色: 自动设置

设置格式[Li]: 字体: (默认) Times New Roman, 小四

218 [fugitive dust \(Text S2\)](#). While the PBL height and WS increase continuously, the Ammonium,
219 EC-aged, and Dust particles begin to decline from 12:00 to 17:00 [LT](#). The subsequent
220 increases of these three particles after 17:00 [LT](#) are attributed to the reduction of PBL height,
221 as a result of the accumulation of pollutants in the near-surface atmosphere.

222 Based on the transport pathways, four air mass clusters are identified to investigate the
223 effect of regional transport on the major particle types (i.e., rich-K, BB, OC, Ammonium,
224 EC-aged, and Dust) (Fig. 2). [Cluster 1, 3 and 4 originated from northeastern Myanmar](#),
225 accounting for 59.8%, 33.2% and 4.6% of the total trajectories, respectively. Cluster 1 had an
226 average percentage of [32.7%](#), [18.5%](#), [12.0%](#), [12.5%](#), [11.1%](#), and [8.9%](#), respectively, on the
227 rich-K, BB, OC, Ammonium, EC-aged, and Dust particles ([Table S1](#)). Clusters 3 and 4 have
228 comparable contributions of BB, OC, Ammonium, and EC-aged to those of Cluster 1, but
229 with a high contribution of Dust, which approximately [16.6%](#) of Clusters 3 and 4 are referred
230 to as dust pollution. The diurnal variations of the BB and OC fractions are similar which
231 rapidly elevate at 07:00 [LT](#) (Fig. S7) due to the increased contribution of biomass burning and
232 vehicle emissions from Cluster 1, Ammonium and EC-aged particles (peak at 07:00 [LT](#))
233 caused by the effect of Cluster 1 and 3 together. The similar diurnal trend of Clusters 3 and 4
234 are both associated with dust contributions, which decrease at 04:00 [LT](#) and increase at noon.
235 The increased nighttime particles could be attributed to the pollutant accumulation with the
236 decreased PBL height. Cluster 2 originate [from northeastern India and passes over](#)
237 Bangladesh. This cluster accounts for only 2.4 % of the total trajectories, in which [~30.8%](#)
238 and [~35.9%](#) are mainly associated with the rich-K and BB particles, respectively. Even
239 though Clusters 2 and 4 are composed of a small fraction of total trajectories (2.4% and 4.6 %,
240 respectively), BB and dust particles are identified as the major pollutants, suggesting
241 significant influences from India and northeastern Myanmar during the campaign.

242 [A more in-depth investigation of the characteristics of the main particle types in the](#)
243 [southeastern Tibet Plateau was conducted during two episode periods when the number](#)
244 [concentration of particles was high \(i.e., E1: from 08:00 LT April 18th to 08:00 LT April 19th,](#)
245 [2018; E2: 17:00 LT April 26th to 02:00 LT April 28th, 2018\) \(Fig. S5\). Even though the two](#)
246 [episodes are contributed by Cluster 1, the chemical components show significant differences](#)

设置格式[Li]: 字体颜色: 自动设置

设置格式[Li]: 字体: (默认) Times New Roman, 小四, 字体颜色: 自动设置

设置格式[Li]: 字体颜色: 自动设置

删除[Li]: es

删除[Online_Group]: The northeastern Myanmar is the main contributing air masses, corresponding to The most dominant air masses are

设置格式[Li]: 字体: (默认) Times New Roman, 小四, 字体颜色: 自动设置

删除[Li]: from northeastern Myanmar

设置格式[Li]: 字体颜色: 自动设置

删除[Li]: 1.2

删除[Li]: 20.2

删除[Li]: 3.7

删除[Li]: 1.8

删除[Li]: 0.9

删除[Li]: 6.5

删除[Online_Group]: d

删除[Li]: 2.2% and 18.2

删除[Online_Group]: d

删除[Li]: 1

删除[Li]: 1.7

设置格式[Li]: 字体颜色: 自动设置

设置格式[Li]: 字体颜色: 自动设置

设置格式[Li]: 字体颜色: 自动设置

设置格式[Li]: 字体颜色: 自动设置

247 (Table 1). During E1, the average fractions of the rich-K, BB, OC, Ammonium, EC-aged, and
248 Dust particle are 29.0%, 11.5%, 8.1%, 17.5%, 10.0% and 20.3%, respectively, different from
249 39.3%, 14.2%, 10.0%, 13.5%, 17.2%, and 1.3% respectively, during E2. It can be seen that
250 the Dust particle is the major changed factor, which is 93.6% lower during E2 than E1,
251 whereas the EC-aged particle shows a reversible of 72.0% higher during E2. The rich-K, BB,
252 and, OC particles show 22.9%-35.5% differences between the two episode periods. For the
253 air mass clusters (Fig. S8), E1 and E2 exhibit minor differences, mostly originating from
254 northern Myanmar and the Sino-Burmese border, but not identical regions. The Dust particles
255 that are much lower during E2 than E1 could be explained by higher WS (on average of $2.7 \pm$
256 1.0 m/s versus 0.4 ± 0.5 m/s) (Fig. S8) and PBL height (771 ± 717 m versus 560 ± 549 m)
257 (Fig. S9). The Dust particles are mainly formed by re-suspension in the local areas. In
258 addition, the quick thrown-up dust belongs to more coarse size particles, which are out of the
259 detection range of the SPAMS. However, due to the larger dust particles deposited more
260 easily under the low WS and the stagnant air conditions during E1, more suspended dust
261 particles of small size fall in the detection range of SPAMS. Moreover, the increased PBL
262 height and WS could speed up the transportation of pollutants from multiple sources (e.g.,
263 traffic and biomass burning emissions) to the observation site, leading to elevate the fraction
264 of EC-aged, rich-K, BB, and OC particles. The decreased Ammonium particle during E2 is
265 potentially explained by the reductions in the secondary pollutant formation with declines of
266 RH (from $73.9\% \pm 23.9\%$ to $53.1\% \pm 14.9\%$), the oxidation capacities [O_3 : from 82.3 ± 5.5
267 ppbv to 76.8 ± 8.4 ppbv; and NO_x : from, 3.9 ± 0.8 to 2.7 ± 0.8 ppb), in comparison to those
268 during E1.

269 **3.2 Characteristics of size distribution and mixing state**

270 The aerodynamic size distributions of all particle types are shown in Fig. 3. According to
271 the characteristics of the average MS (Text S1 and Fig. S3), rich-K, BB, and OC and EC-aged
272 particles originated from the similar sources of vehicle emission or solid-fuel combustion.
273 Their size distribution thus presents within a small-scale (~440 nm) (Fig. 3a). However, the
274 relative percentage of each particle type is distinct with different size ranges, possibly due to
275 the unique atmospheric processing. For example, as shown in Fig. 3b, the proportions of

删除[Li]: Fig. 3 shows t

删除[Li]: each

删除[Li]: Corresponding

删除[Li]: 2

删除[Li]: ,

删除[Online_Group]: have

删除[Online_Group]: from

删除[Online_Group]: ,

删除[Online_Group]: t

删除[Online_Group]: at

删除[Li]: proportion

删除[Online_Group]: under

删除[Li]: s

删除[Online_Group]: maybe

删除[Online_Group]: different

删除[Online_Group]: in ambient

删除[Li]: percentage

rich-K and BB types increases along with the increase in particle size from 200 to 420 nm, but then decrease. OC and EC-aged types are mainly distributed in relatively small particle sizes, and their proportions gradually decrease when the size ranges become larger. Ammonium and Dust types are mainly distributed in large sizes of ~600 nm (Fig. 3a). The proportion of Ammonium particles gradually increases with the increase of particle size and peaks at 740 nm, the relatively large size distribution is ascribed to the intense atmospheric aging during regional transport (Text S1). The proportion of Dust particles gradually increases with a size > 560 nm and peaks at 1.48 μm. This is consistent with the fact that dust is a coarse particle, generally formed at the roadside and fly ash.

Compared with the total particle size distribution, the peak values of the six main particle types show minor differences (< 80 nm) during the two different episode periods (Fig. S10a). In Fig. S10b, a relatively high proportion of the rich-K and BB particles exhibit bimodal distributions, while peaks at < 300 nm are affected by the primary emissions and > 300 nm are associated with the aging process (Li et al., 2022b; Bi et al., 2011). Hence, the percentage of the six particle types distribute in wider size ranges during E2 than during E1, due to the more intensive atmospheric aging. Relatively greater fluctuation for the large-size fractions (> 1.1 μm) could be explained by the low particle concentration (a number less than 20). It should be pointed out that further application of this method would require a co-located particle-sizing instrument to scale the size-resolved particle detection efficiency. Both particle composition and size-dependent are the predominant impacting factors on the particle detection efficiency of the SPAMS (Wenzel et al., 2003; Yang et al., 2017; Healy et al., 2013).

To investigate the mixing state of the secondary species in the six main particle types, the number fractions of six secondary markers ($^{97}\text{HSO}_4^-$, $^{195}\text{H}(\text{HSO}_4)_2^-$, $^{62}\text{NO}_3^-$, $^{18}\text{NH}_4^+$, $^{58}\text{C}_2\text{H}_5\text{NHCH}_2^+$ and $^{89}\text{HC}_2\text{O}_4^-$) are selected (Fig. 4). The presences of amine (m/z $^{58}\text{C}_2\text{H}_5\text{NHCH}_2^+$) and sulfuric acid (m/z $^{195}\text{H}(\text{HSO}_4)_2^-$) signals are possibly indicative of the water uptake (Chen et al., 2019) and acidic property of the particles (Rehbein et al., 2011), respectively. The mixing states are calculated by the ratio of the number concentration of the selected ions to each particle type.

The most abundant of $^{97}\text{HSO}_4^-$ and $^{18}\text{NH}_4^+$ fraction are seen in Ammonium (99% and

删除[Li]: from 17% to 44%

删除[Online_Group]: of

删除[Online_Group]: , and

删除[Online_Group]: s

删除[Li]: to <10% at 900 nm; a similar thing, the percent

删除[Li]: However, the

删除[Li]: percentage of them

删除[Online_Group]: s

删除[Li]: from 31% and 36% to 9%

删除[Online_Group]: (< 500 nm)

删除[Li]: from ~200 to 500 and ~400 nm, respectively

删除[Li]: Notably, the

删除[Li]: The

删除[Li]: from 1.6% to 29%

删除[Li]: from 440 to

删除[Li]: , then decline to <10% at 1.2 μm. T

删除[Li]: of the Ammonium type

删除[Li]: percentage

删除[Online_Group]: from in

删除[Online_Group]: the

删除[Li]: 10% at

删除[Li]: to 60% at

删除[Online_Group]: consist to

删除[Online_Group]: the

删除[Li]: In terms of

删除[Online_Group]: s

删除[Li]: rich-K, BB, and EC-aged

删除[Li]: between two episode periods (Fig. 5a)

删除[Li]: Expressed i

删除[Li]: relative proportion (

删除[Li]: 5

删除[Li]: b)

删除[Online_Group]: a

删除[Li]: In addition

94%, *respectively*) and EC-aged (92% and 31%, *respectively*) particles, *whereas much low fraction of* $^{62}\text{NO}_3^-$ is *found* (2% and 7%, *respectively*). *These* suggest that ammonium sulfate is not a predominant form instead of ammonium nitrate (Zhang et al., 2013). The high contribution of sulfate in EC-containing particles also *suggests a significant influence of anthropogenically emitted sulfate precursors* (e.g., SO_2) on the aging of EC-containing particles at the high altitude (Peng et al., 2016; Zhang et al., 2017a). Meanwhile, *relatively high number fractions* of $^{195}\text{H}(\text{HSO}_4)_2^-$ and $^{58}\text{C}_2\text{H}_5\text{NHCH}_2^+$ are also observed in Ammonium (63% and 60%) and EC-aged (4% and 19%) particles. These abundant mixtures *potentially* represent the high hygroscopicity of Ammonium and EC-aged particles, and their ability to neutralize the acidic particles of Ammonium particle (Sorooshian et al., 2007). Then, a moderate *fraction* of $^{97}\text{HSO}_4^-$ and $^{18}\text{NH}_4^+$ are seen on the rich-K (65%, 7%) and OC (56%, 4%) particles. In contrast, more $^{62}\text{NO}_3^-$ contribute to the rich-K (38%) and OC (68%) particles, mainly affected by vehicle emissions (Text S1). Following BB (18%) and Dust (6%) particles are found *in a relatively low number fraction* of $^{97}\text{HSO}_4^-$, *while* the moderate $^{62}\text{NO}_3^-$ accounts for 45% of the BB particle *but* only 3% of the Dust particle. *Besides, the number fraction of* $^{18}\text{NH}_4^+$ is minor (<1%), which *suggests the aging degree* of BB and Dust particles *is relatively low*. In addition, *oxalate* ($^{89}\text{HC}_2\text{O}_4^-$), *a representative component* of secondary organic formation, is mainly mixed with BB (13%) and rich-K (12%) particles. *This is because the substantial precursors of oxalic acid, including acetate* ($^{59}\text{C}_2\text{H}_3\text{O}_2^-$), *methylglyoxal* ($^{71}\text{C}_3\text{H}_3\text{O}_2^-$), *glyoxylate* ($^{73}\text{C}_2\text{HO}_3^-$), *are emitted from biomass burning, while oxalate heterogeneously formed in BB related particles* (Zhang et al., 2019b; Zauscher et al., 2013). A relatively low fraction (<5%) of the oxalate-containing particles in OC, Ammonium, EC-aged and Dust particles *potentially limited by the contributions of precursor oxalic acid*.

Compared to the individual particle mixing state in urban or suburban areas that are located close to emission sources (Chen et al., 2016; Dall'Osto and Harrison, 2012; Zhang et al., 2017a; Li et al., 2022b), the high fractions of sulfate and ammonium at the high altitude area *demonstrate a high degree of aging of the individual particles, whereas the low fraction of nitrate with high volatility indicates its loss during transportation processing*.

The number fractions of six markers in the four clusters were used to further investigate the impacts of regional transport. As shown in Fig. 5a and c, the dominant mixing ion types in

删除[Online_Group]: but

删除[Online_Group]: the proportionfraction of

删除[Online_Group]:

删除[Online_Group]: lower

删除[Online_Group]: ,

删除[Online_Group]: indicates

删除[Online_Group]: ssions

删除[Online_Group]: of

设置格式[Li]: 字体: (默认) Times New Roman, 小四 ...

设置格式[Li]: 字体颜色: 自动设置

删除[Online_Group]: a

删除[Li]: DEA

删除[Online_Group]: is

删除[Online_Group]: may

删除[Li]: ity

删除[Li]: proportion

删除[Online_Group]: s

删除[Online_Group]: ed

删除[Online_Group]: by

删除[Online_Group]: and

删除[Online_Group]: ,

删除[Online_Group]: and

删除[Online_Group]: is

删除[Online_Group]: ed

删除[Online_Group]: aging are

删除[Online_Group]: ing

删除[Online_Group]: the

删除[Online_Group]: , oxalate ($^{89}\text{HC}_2\text{O}_4^-$)

删除[Online_Group]: ,

删除[Online_Group]: were

设置格式[Li]: 字体: (默认) Times New Roman, 小四 ...

删除[Online_Group]: then

设置格式[Li]: 字体颜色: 自动设置

删除[Online_Group]: produc

336 each particles (except for Dust type) are similar among the four Clusters. For Cluster 1, the
337 number fractions of $^{97}\text{HSO}_4^-$ and $^{89}\text{HC}_2\text{O}_4^-$ have larger values in five particle types (except
338 for Dust type) than those in other clusters. Similar to Cluster 1, 3 and 4 are impacted by
339 regional transport from northeastern Myanmar. Moreover, the fractions of the six markers are
340 similar in OC, Ammonium, and EC-aged types. However, $^{97}\text{HSO}_4^-$ is decreased in rich-K,
341 BB and Dust types, while $^{62}\text{NO}_3^-$ is increased in rich-K, and decreased in Dust types. As
342 discussed in Section 3.1, these phenomena demonstrate that the aging degree of Cluster 3 and
343 4 might be lower than that of Cluster 1. For Cluster 2, the fraction of $^{97}\text{HSO}_4^-$ is obviously
344 decreased in rich-K, BB and EC-aged types but slightly increased in Dust type (Fig. 5f). Such
345 pattern inverse the observations in rich-K, OC and Dust types for $^{62}\text{NO}_3^-$ ions. These
346 variations in Cluster 2 are more likely due to influences of biomass-burning activities from
347 the surrounding area of the sampling site, rather than regional transport. Furthermore, Cluster
348 2 is associated with regional transport from northeastern India along the afternoon to
349 nighttime (from 15:00 LT on 11 May to 07:00 LT on 12 May), which is favorable to the
350 nitrate formation N_2O_5 by heterogeneous hydrolysis (Wang et al., 2017; Ding et al., 2021).
351 However, these cases are infrequent, as only 2% of trajectories are associated with Cluster 2.

352 During E1, more than 50% of $^{97}\text{HSO}_4^-$ fractions are mixed in the rich-K (81%), OC
353 (62%), Ammonium (100%), EC-aged (98%) particles (Fig. S11), lower than in BB (37%) and
354 Dust (4%) particles. Dissimilar with E1, the number fraction of $^{97}\text{HSO}_4^-$ increases to 34%
355 during E2, potentially associated with the enhancement by secondary formation. However,
356 the mixing state of $^{15}\text{H}(\text{HSO}_4)_2^-$, $^{62}\text{NO}_3^-$, NH_4^+ and oxalate fractions are similar between the
357 two episodes events. The fractions of $^{58}\text{C}_2\text{H}_5\text{NHCH}_2^+$ are significantly higher in E2 than E1
358 for Ammonium (67% versus 31%) and EC-aged particles (48% versus 17%), due to the
359 relatively higher hygroscopic behavior (i.e., RHs) (Sorooshian et al., 2007).

360 3.3 Formation process of the high number concentration particle episodes

361 Photochemical oxidation and aqueous-phase reaction are the key formation pathways of
362 secondary species (Link et al., 2017; Xue et al., 2014; Jiang et al., 2019). Generally, the
363 oxidant O_x ($\text{O}_3 + \text{NO}_2$) concentration and RH serve as indicators of the degree of
364 photochemical oxidation (Wood et al., 2010) and aqueous-phase reaction (Ervens et al., 2011).
365 In this study, the relative number fractions of $^{43}\text{C}_2\text{H}_3\text{O}^+$, $^{89}\text{HC}_2\text{O}_4^-$, $^{62}\text{NO}_3^-$, $^{97}\text{HSO}_4^-$, and

删除[Online_Group]: were

删除[Online_Group]: for

设置格式[Li]: 字体颜色: 自动设置, 下标

设置格式[Li]: 字体颜色: 自动设置

删除[Online_Group]: d

删除[Online_Group]: compared with

删除[Online_Group]: with

删除[Online_Group]: Cluster

删除[Online_Group]: were

设置格式[Li]: 字体: (默认) Times New Roman, 小四

删除[Online_Group]: also associated with

设置格式[Li]: 字体颜色: 自动设置

删除[Online_Group]: ,

设置格式[Li]: 字体: (默认) Times New Roman, 小四

设置格式[Li]: 字体颜色: 自动设置

删除[Online_Group]: mixing have the similar mixed

设置格式[Li]: 字体: (默认) Times New Roman, 小四

删除[Online_Group]: But

设置格式[Li]: 字体颜色: 自动设置

删除[Online_Group]: was

设置格式[Li]: 字体: (默认) Times New Roman, 小四

设置格式[Li]: 字体颜色: 自动设置

删除[Online_Group]: was

删除[Online_Group]: type

删除[Online_Group]: .

设置格式[Li]: 字体: (默认) Times New Roman, 小四

设置格式[Li]: 字体颜色: 自动设置

删除[Online_Group]: ay

设置格式[Li]: 字体: (默认) Times New Roman, 小四

设置格式[Li]: 字体颜色: 自动设置

设置格式[Li]: 字体: (默认) Times New Roman, 小四

设置格式[Li]: 字体颜色: 自动设置

删除[Online_Group]: wa

删除[Online_Group]: and

366 $^{18}\text{NH}_4^+$ -containing particles to the total detected particles were selected to indicate the
367 secondary formation (Liang et al., 2022). The correlations of the number fraction of each
368 secondary species with the O_x concentrations (O_x) during daytime (from 06:00 to 20:00 LT)
369 and RH during nighttime (from 20:00 to 06:00 next day LT) are used to present the formation
370 pathways during the two episodes (Li et al., 2022).

371 As illustrated in Fig. 6, for E1, $^{43}\text{C}_2\text{H}_3\text{O}^+$, $^{89}\text{HC}_2\text{O}_4^-$, $^{97}\text{HSO}_4^-$, $^{18}\text{NH}_4^+$ show significant
372 negative linear correlations with O_x ($p < 0.01$), and the correlation strengths range from
373 moderate to strong ($r = -0.51$ to -0.81). However, the $^{62}\text{NO}_3^-$ fraction shows an upward trend
374 with an insignificant correlation, ($r = 0.33$, $p > 0.05$) with the increase in O_x concentration. For
375 E2, $^{43}\text{C}_2\text{H}_3\text{O}^+$ shows weak correlation with O_x ($r = 0.37$, $p > 0.05$), but strong correlations
376 with $^{89}\text{HC}_2\text{O}_4^-$, $^{97}\text{HSO}_4^-$, and $^{18}\text{NH}_4^+$ ($r = 0.81\sim 0.92$, $p < 0.01$). It should be noted that $^{62}\text{NO}_3^-$
377 has a strong negative correlation ($r = -0.85$, $p < 0.01$) with O_x . In general, the opposite linear
378 relationship between secondary aerosol and O_x during E1 and E2 might be influenced by
379 reasons of i) the relatively low secondary formations because of the small amount of
380 precursors emitting from anthropogenic activities around the sampling site (Li et al., 2016); ii)
381 higher dilution rate of the particles formed in the atmosphere with the rapid rise of PBL
382 height during E1 than E2 (Fig. S12a); iii) the degrees of contributions of regional transport
383 due to the low WS ($0.5 \pm 0.6 \text{ m s}^{-1}$) during E1 and the high WS ($3.1 \pm 1.0 \text{ m s}^{-1}$) during E2,
384 respectively (Fig. S8). Therefore, for E1, the increases of NO_3^- fraction could be influenced
385 by the local nitrate formation, while the declines of other secondary components should be
386 ascribed to the reduced contribution of regional transport. For E2, the decreased of NO_3^-
387 fraction could be caused by the relatively higher volatilization loss of nitrate than other
388 components through the regional transport. Previous study proves that the formations of
389 organic nitrate species (such as $^{27}\text{CHN}^+$, $^{30}\text{NO}^+$, $^{43}\text{CHO}_1\text{N}^+$, and CHO_xN^+) through the
390 $\text{NO}+\text{RO}_2$ pathway dominate 80% of the total nitrate production in tropical forested regions
391 during summertime (Alexander et al., 2009). Aruffo et al (2022) also found that low NO_x (i.e.,
392 $< 6 \text{ ppbv}$), compared to $2.3 \pm 0.8 \text{ ppbv}$ in this study, could even promote the particle-phase
393 partitioning of the lower volatility of organonitrates. These results suggest that
394 photo-oxidation reactions could promote secondary formation, among which the rate of
395 HSO_4^- formation (slope=0.017) is the highest. Increased with O_x concentration during E2, the

删除[Online_Group]: to

删除[Online_Group]: , respectively

删除[Li]: between

删除[Online_Group]: oxidant

删除[Li]: = $\text{O}_3 + \text{NO}_2$

删除[Online_Group]: a.m.

删除[Online_Group]: p.m.

删除[Online_Group]: p.m.

删除[Online_Group]: a.m.

删除[Online_Group]: reflectre

删除[Li]: event

删除[Li]: Chen

删除[Li]: 16

设置格式[Li]: 字体: (默认) Times New Roman, 小四

删除[Online_Group]: shown

设置格式[Li]: 字体颜色: 自动设置

删除[Li]: 7

删除[Li]: compared with E1 and E2, the linear relationsl

删除[Li]: During

删除[Online_Group]: ~

删除[Li]: ,

删除[Li]: except that

删除[Online_Group]: but

删除[Online_Group]: un

删除[Li]: a certain higher but has no significant correlatio

删除[Online_Group]: of

设置格式[Li]: 字体: (默认) Times New Roman, 小四

删除[Online_Group]: has less significant

设置格式[Li]: 字体颜色: 自动设置

删除[Online_Group]: with

设置格式[Li]: 字体: (默认) Times New Roman, 小四

设置格式[Li]: 字体: (默认) Times New Roman, 小四

设置格式[Li]: 字体: (默认) Times New Roman, 小四

删除[Li]: This

396 concentration levels of secondary organic species of $C_2H_3O^+$ (18%-28%) imperceptibly rise,
397 while the oxalate fraction significantly increase by 7%-20% as well. The results indicate that
398 the secondary organic species have different formation capacities through atmospheric
399 oxidation.

400 Considering that the oxalate is abundant, mixed in rich-K (14%), BB (15%), EC-aged
401 (5%), and Dust (6%) particles in Cluster 1 (Fig. 5), and the increased contributions of rich-K
402 (39.3%), BB (14.2%) and EC-aged (17.2%) types during E2 (Table 1), the apparent formation
403 of oxalate might be due to the enhancement of regional transport. Particularly, this presents
404 the nearby biomass burning and combustion activities produce more precursor species of
405 oxalate (Sullivan et al., 2007; Kundu et al., 2010; Zhang et al., 2017b).

406 Fig. 7 illustrates that the number fractions of $^{43}C_2H_3O^+$, $^{89}HC_2O_4^-$, $^{97}HSO_4^-$, and $^{18}NH_4^+$
407 have moderate to strong positive correlations with RH ($r = 0.70\sim 0.81$, $p < 0.01$ or 0.05) in the
408 nighttime during the two episodes, except that $^{43}C_2H_3O^+$ during E2 ($p = 0.48$) and $^{89}HC_2O_4^-$
409 during E1 ($p = 0.12$). Furthermore, $^{62}NO_3^-$ fraction has no obvious changes with insignificant
410 correlation with RH during E1 ($p = 0.43$) and presents a moderate negative correlation with
411 RH ($r = 0.69$, $p < 0.01$) during E2. As shown in Fig. 7e, the highest aqueous formation rate of
412 HSO_4^- is mainly due to the properties of low volatile and high hygroscopic of sulfate (Wang
413 et al., 2016; Zhang et al., 2019c; Sun et al., 2013). Compared with that during E2
414 (slop=0.014), the decreased formation rate of HSO_4^- during the E1 (slop=0.009) may be
415 because the decreases of aerosol acidity in higher RH > 80% (Huang et al., 2019; Meng et al.,
416 2014; Tian et al., 2021). And the increased contributions of regional transport due to the high
417 WS (2.4 ± 0.8 m s $^{-1}$) during E2 are comparable to the low WS (0.08 ± 0.08 m s $^{-1}$) during E1
418 (Fig. S8). The fair production rate of NH_4^+ during the E1 (slop= 0.005) and E2 (slop=0.006)
419 demonstrate that an aqueous-phase reaction could effectively promote ammonium formation.
420 Meanwhile, a slightly larger slop during E2 could be also affected by the increased
421 contributions of regional transport. Compared with those during E1, the inverse generation
422 rates of two secondary organic species (i.e., $C_2H_3O^+$ and $HC_2O_4^-$), during E2 are possibly
423 caused by the different formation pathways with a variety of RH levels or distinct regional
424 transports. For example, $C_2H_3O^+$ shows a strong correlation with RH ($r = 0.70$, $p < 0.05$)
425 during E1 (slop=0.003) but has insignificant correlation during E2. This could be explained

删除[Online_Group]: a

删除[Online_Group]: and

删除[Li]: also

删除[Online_Group]: s

删除[Online_Group]: isat

删除[Online_Group]: s

删除[Li]: result shows

删除[Online_Group]: were

删除[Li]: a

删除[Online_Group]: in the capacity of

删除[Online_Group]: formation

删除[Li]: ,

设置格式[Li]: 字体: (默认) Times New Roman, 小四

设置格式[Li]: 字体颜色: 自动设置

设置格式[Li]: 字体: (默认) Times New Roman, 小四

设置格式[Li]: 字体颜色: 自动设置

设置格式[Li]: 字体: (默认) Times New Roman, 小四

设置格式[Li]: 字体颜色: 自动设置

设置格式[Li]: 字体: (默认) Times New Roman, 小四

删除[Online_Group]: Combining the results of oxalate

设置格式[Li]: 字体颜色: 自动设置

设置格式[Li]: 字体: (默认) Times New Roman, 小四

设置格式[Li]: 字体颜色: 自动设置

设置格式[Li]: 字体: (默认) Times New Roman, 小四

设置格式[Li]: 字体颜色: 自动设置

删除[Li]: formation of ammonium oxalate by adsorption

删除[Li]: 8

删除[Li]: event

删除[Online_Group]: in nighttime

删除[Online_Group]: also

删除[Online_Group]: and

删除[Li]: 8

删除[Li]: is higher during the E1 (slop is 0.014) than in E

设置格式[Li]: 字体: (默认) Times New Roman, 小四

426 by high RHs that could effectively promote secondary organic formation during E1. In
427 addition, the HC_2O_4^- fraction increases slightly (9.7-13.1%), during E1 is potentially ascribed
428 to more abundant Dust-type particles (20.3%) which compose of high calcium (Ca) (Fig. S13)
429 that favor the formation of metal oxalate complexes (i.e., Ca oxalate). At high RHs ($93.4 \pm$
430 7.6%), if oxalate ions are dissolved in the aqueous phase with the presence of Ca ions, the Ca
431 oxalate complexes can precipitate because of their low hygroscopic and insoluble natures
432 (Furukawa and Takahashi, 2011). This could offset the oxalate formation in the
433 aqueous-phase reaction. However, significant linear increases (slope=0.003), with RH ($r = 0.81,$
434 $p < 0.01$) during E2 demonstrate that the aqueous-phase reaction effectively promotes the
435 oxalate formation (Cheng et al., 2017; Meng et al., 2020). No obvious change and
436 insignificant correlation between $^{62}\text{NO}_3^-$ and RH are found during E1, potentially attributed
437 to the decreases of NO_2 concentration (3.7 ± 0.4 ppbv) in the local atmosphere. Meanwhile,
438 high RHs could promote organonitrates formation (Fang et al., 2021; Fry et al., 2014). The
439 linearity between $^{62}\text{NO}_3^-$ and RH ($r = 0.69, p < 0.01$) significantly decreases during E2,
440 mostly due to the losses of the volatile compound through the regional transport (Fig. S14).

441 **4 Conclusions**

442 This study presents the chemical composition, size distribution, mixing state, and
443 secondary formation of individual particles in the southeastern margin of TP, China during
444 the pre-monsoon season using a high-resolution SPAMS. The finding shows that the rich-K
445 (30.9%) and BB types (18.7%) are the two dominant aerosol particles in the remote area;
446 followed by the OC (12.8%), Ammonium (11.9%), EC-aged (10.9%), and Dust (10.7%) types;
447 the NaK-SN, Metal and Others types contributed 0.3–2.8% to the total ambient particles. By
448 interpreting the mass spectra and diurnal trends, the major particle types are mainly from
449 traffic emission, biomass burning, secondary formation, and fly ash, while the dynamics of
450 the PBL height could also affect the contributions of these particles. The observed change in
451 the number fraction of the particle types was mainly influenced by air mass (97.61% of the
452 total trajectories) from northeastern Myanmar, and significantly contributed to rich-K and BB
453 types. The particle types show distinct size distributions. The two most critical particle types
454 of rich-K and BB appear in a unimodal pattern, the fractions of OC and EC-aged gradually
455 decrease with the increase of the particle sizes, but Ammonium and Dust types show the

设置格式[Li]: 字体: (默认) Times New Roman, 小四

删除[Online_Group]: (主要是 Ca) . However, t

设置格式[Li]: 字体颜色: 自动设置

删除[Li]: has a slight

删除[Li]: higher

删除[Online_Group]: d

删除[Online_Group]: %

删除[Online_Group]:

设置格式[Li]: 字体: (默认) Times New Roman, 小四

设置格式[Li]: 字体颜色: 自动设置

设置格式[Li]: 字体: (默认) Times New Roman, 小四

设置格式[Li]: 字体颜色: 自动设置

设置格式[Li]: 字体: (默认) Times New Roman, 小四

设置格式[Li]: 字体颜色: 自动设置

设置格式[Li]: 字体颜色: 自动设置, 非突出显示

设置格式[Li]: 字体颜色: 自动设置

设置格式[Li]: 字体: (默认) Times New Roman, 小四

设置格式[Li]: 字体颜色: 自动设置

设置格式[Li]: 字体: (默认) Times New Roman, 小四

设置格式[Li]: 字体颜色: 自动设置

删除[Li]: the

设置格式[Li]: 字体: (默认) Times New Roman, 小四

设置格式[Li]: 字体颜色: 自动设置

设置格式[Li]: 字体: (默认) Times New Roman, 小四

设置格式[Li]: 字体颜色: 自动设置

设置格式[Li]: 字体: (默认) Times New Roman, 小四

设置格式[Li]: 字体颜色: 自动设置

设置格式[Li]: 字体: (默认) Times New Roman, 小四

设置格式[Li]: 字体颜色: 自动设置

设置格式[Li]: 字体: (默认) Times New Roman, 小四

设置格式[Li]: 字体颜色: 自动设置

设置格式[Li]: 字体: (默认) Times New Roman, 小四

设置格式[Li]: 字体颜色: 自动设置

设置格式[Li]: 字体: (默认) Times New Roman, 小四

456 opposite. Sulfate is the major secondary species and is highly mixed with rich-K, Ammonium,
457 and EC-aged types. Nitrate has a relatively low mixing ratio due to its higher volatility than
458 sulfate during regional transportation, except for BB and OC types. During the entire study
459 campaign, two air episodes with the high number concentration particle occurred but with
460 significant differences in each particle fraction due to the different meteorological conditions
461 (RH, WS, etc.). The indicators of secondary formation, $C_2H_3O^+$, $HC_2O_4^-$, NH_4^+ , NO_3^- and
462 HSO_4^- are shown inverse linear correlation with O_x (O_3+NO_2) during episode I and II
463 periods due to the different meteorological conditions; however, they are present a positive
464 linear correlation with relative humidity (RH), except for NO_3^- shown the negative linear
465 correlation with RH due to the low precursors concentration and potential organonitrates
466 formation. These results demonstrated that the capacity of atmospheric aging of
467 photo-oxidation and aqueous reaction have complex influencing factors. The results of this
468 study provide useful information concerning the detailed characteristic of aerosol components,
469 size distribution, and mixing states in the southeast TP, and highlight the importance of the
470 cross-border transport and formation mechanism of aerosols in high-altitude regions.

删除[Li]: The results of the formation mechanism of secondary species demonstrate that the formation capacity of atmospheric oxidation is affected by the PBL height, but the relative humidity (RH) could promote the formation of secondary species, especially $^{97}HSO_4^-$ and $^{18}NH_4^+$.

471 *Data availability.* The data presented in this study are available at the Zenodo data archive
472 <https://doi.org/10.5281/zenodo.7336857>.

473

474 *Competing interests.* The authors declare that they have no conflict of interest.

475

476 *Author contributions.* QW and JC designed the campaign. WR conducted field measurements.
477 LL, QW, JT, and YZ made data analysis and interpretation. LL and QW wrote the paper. All
478 the authors reviewed and commented on the paper.

479

480 *Acknowledgments.* The authors are grateful to the staff from Lijiang Astronomical Station for
481 their assistance with field sampling. The authors are also grateful to Weikang Ran, Yonggang
482 Zhang, and other staff for the field observation.

483

484 *Financial support.* This work was supported by [the Second Tibetan Plateau Scientific](#)
485 [Expedition and Research Program \(STEP\) \(2019QZKK0602\)](#), [the National Natural Science](#)
486 [Foundation of China \(41877391\)](#), and the Youth Innovation Promotion Association of the
487 Chinese Academy of Sciences (2019402).

删除[Li]: the National Natural Science Foundation of China
(41877391)

删除[Li]: the Second Tibetan Plateau Scientific Expedition
and Research Program (STEP) (2019QZKK0602)

488

489 Reference

490 Alexander, B., Hastings, M. G., Allman, D. J., Dachs, J., Thornton, J. A., and Kunasek, S. A.: Quantifying
491 atmospheric nitrate formation pathways based on a global model of the oxygen isotopic composition
492 ($\Delta^{17}\text{O}$) of atmospheric nitrate, *Atmos. Chem. Phys.*, 9, 5043–5056,
493 <https://doi.org/10.5194/acp-9-5043-2009>, 2009.

494 Aruffo, E., Wang, J., Ye, J., Ohno, P., Qin, Y., Stewart, M., McKinney, K., Di Carlo, P., and Martin, S. T.:
495 Partitioning of Organonitrates in the Production of Secondary Organic Aerosols from α -Pinene
496 Photo-Oxidation, *Environ. Sci. Technol.*, 56, 5421–5429, <https://doi.org/10.1021/acs.est.1c08380>,
497 2022.

删除[Li]: Angelino, S., Suess, D. T., and Prather, K. A.:
Formation of aerosol particles from reactions of secondary and
tertiary alkylamines: characterization by aerosol time-of-flight
mass spectrometry, *Environ. Sci. Technol.*, 35, 3130–3138,
<https://doi.org/10.1021/es0015444>, 2001.

498 Bi, X. H., Zhang, G. H., Li, L., Wang, X. M., Li, M., Sheng, G. Y., Fu, J. M., and Zhou, Z.: Mixing state of
499 biomass burning particles by single particle aerosol mass spectrometer in the urban area of PRD,
500 China, *Atmos. Environ.*, 45, 3447–3453, <https://doi.org/10.1016/j.atmosenv.2011.03.034>, 2011.

501 Bi, X. H., Lin, Q. H., Peng, L., Zhang, G. H., Wang, X. M., Brechtel, F. J., Chen, D. H., Li, M., Peng, P. A.,
502 Sheng, G. Y., and Zhou, Z.: In situ detection of the chemistry of individual fog droplet residues in the
503 Pearl River Delta region, China, *J. Geophys. Res. Atmos.*, 121, 9105–9116,
504 <https://doi.org/10.1002/2016jd024886>, 2016.

505 Budisulistiorini, S. H., Riva, M., Williams, M., Chen, J., Itoh, M., Surratt, J. D., and Kuwata, M.:

506 Light-absorbing brown carbon aerosol constituents from combustion of Indonesian peat and biomass,
507 Environ. Sci. Technol., 51, 4415-4423, <https://doi.org/10.1021/acs.est.7b00397>, 2017.

508 Canagaratna, M. R., Jayne, J. T., Jimenez, J. L., Allan, J. D., Alfarra, M. R., Zhang, Q., Onasch, T. B.,
509 Drewnick, F., Coe, H., Middlebrook, A., Delia, A., Williams, L. R., Trimborn, A. M., Northway, M. J.,
510 DeCarlo, P. F., Kolb, C. E., Davidovits, P., and Worsnop, D. R.: Chemical and microphysical
511 characterization of ambient aerosols with the aerodyne aerosol mass spectrometer, Mass Spectrom.
512 Rev., 26, 185–222, <https://dx.doi.org/10.1002/mas.20115>, 2007.

513 [Chan, C. Y., Wong, K. H., Li, Y. S., Chan, Y., and Zhang, X.D.: The effects of Southeast Asia fire activities](#)
514 [on tropospheric ozone, trace gases and aerosols at a remote site over the Tibetan Plateau of Southwest](#)
515 [China, Tellus B, 58B, 310–318, <https://doi.org/10.1111/j.1600-0889.2006.00187.x>, 2017.](#)

516 [Chen, Y., Cao, J. J., Huang, R. J., Yang, F. M., Wang, Q. Y., and Wang, Y. C.: Characterization, mixing](#)
517 [state, and evolution of urban single particles in Xi'an \(China\) during wintertime haze days, Sci. Total](#)
518 [Environ., 573, 937–945, <https://doi.org/10.1016/j.scitotenv.2016.08.151>, 2016.](#)

519 Chen, Y., Wenger, J. C., Yang, F. M., Cao, J. J., Huang, R. J., Shi, G. M., Zhang, S. M., Tian, M., and Wang,
520 H. B.: Source characterization of urban particles from meat smoking activities in Chongqing, China
521 using single particle aerosol mass spectrometry, Environ. Pollut., 228, 92–101,
522 <https://doi.org/10.1016/j.envpol.2017.05.022>, 2017.

523 Chen, Y., Tian, M., Huang, R. J., Shi, G. M., Wang, H. B., Peng, C., Cao, J. J., Wang, Q. Y., Zhang, S. M.,
524 Guo, D. M., Zhang, L. M., and Yang, F. M.: Characterization of urban amine-containing particles in
525 southwestern China: seasonal variation, source, and processing, Atmos. Chem. Phys., 19, 3245–3255,
526 <https://doi.org/10.5194/acp-19-3245-2019>, 2019.

527 Chen, J. Q., and Bordoni, S.: Orographic effects of the Tibetan Plateau on the East Asian Summer
528 Monsoon: An energetic perspective, J. Climate., 27, 3052–3072,
529 <https://doi.org/10.1175/JCLI-D-13-00479.1>, 2014.

530 [Cheng, C. L., Li, M., Chan, C. K., Tong, H. J., Chen, C. H., Chen, D. H., Wu, D., Li, L., Wu, C., Cheng, P.,](#)
531 [Gao, W., Huang, Z. X., Li, X., Zhang, Z. J., Fu, Z., Bi, Y. R., Zhou, Z.: Mixing state of acid](#)
532 [containing particles in the rural area of Pearl River Delta, China: implication of the formation mechanism](#)
533 [of oxalic acid, Atmos. Chem. Phys., 17, 9519–9533, <https://doi.org/10.5194/acp-17-9519-2017>, 2017.](#)

534 Crippa, M., DeCarlo, P. F., Slowik, J. G., Mohr, C., Heringa, M. F., Chirico, R., Poulain, L., Freutel, F.,
535 Sciare, J., Cozic, J., Di Marco, C. F., Elsasser, M., Nicolas, J. B., Marchand, N., Abidi, E.,
536 Wiedensohler, A., Drewnick, F., Schneider, J., Borrmann, S., Nemitz, E., Zimmermann, R., Jaffrezo, J.
537 L., Prévôt, A. S. H., and Baltensperger, U.: Wintertime aerosol chemical composition and source
538 apportionment of the organic fraction in the metropolitan area of Paris, Atmos. Chem. Phys., 13,
539 961–981, <https://doi.org/10.5194/acp-13-961-2013>, 2013.

540 Dall'Osto, M., Beddows, D.C.S., Gietl, J. K., Olatunbosun, O. A., Yang, X. G., and Harrison, R. M.:
541 Characteristics of tyre dust in polluted air: studies by single particle mass spectrometry (ATOFMS),
542 Atmos. Environ. 94, 224–230, <https://doi.org/10.1016/j.atmosenv.2014.05.026>, 2014.

543 Dall'Osto, M., and Harrison, R. M.: Urban organic aerosols measured by single particle mass spectrometry
544 in the megacity of London, Atmos. Chem. Phys., 12, 4127–4142,
545 <http://dx.doi.org/10.5194/acp-12-4127-2012>, 2012.

546 [Ding, J., Dai, Q. L., Zhang, Y. F., Xu, J., Huangfu, Y. Q., Feng, Y. C.: Air humidity affects secondary](#)
547 [aerosol formation in different pathways, Sci. Total Environ., 759, 143540–143549,](#)
548 [https://doi.org/10.1016/j.scitotenv.2020.143540, 2021.](#)

549 [Draxler, R. and Hess, G.: An overview of the HYSPLIT_4 modelling system for trajectories, Aust.](#)

删除[Li]: Cao, J. J., Tie X. X., Xu B., Zhao, Z. Z., Zhu, C (...)

删除[Li]: Chen, P. F., Shichang Kang, S. C., Bai, J. K., (...)

设置格式[Li]: 字体: (默认) Times New Roman, (中 (...)

设置格式[Li]: 字体颜色: 自动设置

设置格式[Li]: 字体: (默认) Times New Roman, (中 (...)

设置格式[Li]: 字体颜色: 自动设置

设置格式[Li]: 字体: (默认) Times New Roman, (中 (...)

设置格式[Li]: 字体颜色: 自动设置

设置格式[Li]: 字体: (默认) Times New Roman, (中 (...)

设置格式[Li]: 字体颜色: 自动设置

设置格式[Li]: 字体: (默认) Times New Roman, (中 (...)

设置格式[Li]: 字体颜色: 自动设置

设置格式[Li]: 字体: (默认) Times New Roman, (中 (...)

设置格式[Li]: 字体颜色: 自动设置

设置格式[Li]: 字体: (默认) Times New Roman, (中 (...)

设置格式[Li]: 字体颜色: 自动设置

设置格式[Li]: 字体: (默认) Times New Roman, (中 (...)

设置格式[Li]: 字体颜色: 自动设置

设置格式[Li]: 字体: (默认) Times New Roman, (中 (...)

设置格式[Li]: 字体颜色: 自动设置

设置格式[Li]: 字体: (默认) Times New Roman, (中 (...)

设置格式[Li]: 字体颜色: 自动设置

设置格式[Li]: 字体: (默认) Times New Roman, (中 (...)

设置格式[Li]: 字体颜色: 自动设置

设置格式[Li]: 字体颜色: 自动设置

设置格式[Li]: 字体颜色: 自动设置

550 [Meteorol. Mag., 47, 295–308, 1998.](#)

551 Du, W., Sun, Y. L., Xu, Y. S., Jiang, Q., Wang, Q. Q., Wang, W., Wang, F., Bai, Z. P., Zhao, X. D., and

552 Yang, Y. C.: Chemical characterization of submicron aerosol and particle growth events at a national

553 background site (3295 m a.s.l.) on the Tibetan Plateau, *Atmos. Chem. Phys.*, 15, 10811–10824,

554 <https://doi.org/10.5194/acp-15-10811-2015>, 2015.

555 Engling, G., Zhang, Y. N., Chan, C. Y., Sang, X. F., Lin, M., Ho, K. F., Li, Y. S., Lin, C. Y., and Lee, J. J.:

556 Characterization and sources of aerosol particles over the southeastern Ti-betan Plateau during the

557 Southeast Asia biomass-burning season, *Tellus B*, 63, 117–128,

558 <https://doi.org/10.1111/j.1600-0889.2010.00512.x>, 2011.

559 Ervens, B., Turpin, B. J., and Weber, R. J.: Secondary organic aerosol formation in cloud droplets and

560 aqueous particles (aqSOA): a review of laboratory, field and model studies, *Atmos. Chem. Phys.*, 11,

561 11069–11102, <https://doi.org/10.5194/acp-11-11069-2011>, 2011.

562 Fang, X. Z., Liu, Y. Y., Li, K. J., Wang, T., Deng, Y., Feng, Y. Q., Yang, Y., Cheng, H. Y., Chen, J. M., and

563 Zhang, L. W.: Atmospheric Nitrate Formation through Oxidation by Carbonate Radical, *ACS Earth*

564 *Space Chem.*, 5, 1801–1811, <https://doi.org/10.1021/acsearthspacechem.1c00169>, 2021.

565 Fry, J. L., Draper, D. C., Barsanti, K. C., Smith, J. N., Ortega, J., Winkler, P. M., Lawler, M. J., Brown, S.

566 S., Edwards, P. M., Cohen, R. C., and Lee, L.: Secondary Organic Aerosol Formation and Organic

567 Nitrate Yield from NO₃ Oxidation of Biogenic Hydrocarbons, *Environ. Sci. Technol.*, 48,

568 11944–11953, <https://doi.org/10.1021/es502204x>, 2014.

569 [Furukawa, T. and Takahashi, Y.: Oxalate metal complexes in aerosol particles: implications for the](#)

570 [hygroscopicity of oxalate-containing particles. *Atmos. Chem. Phys.*, 11, 4289 – 4301,](#)

571 <https://doi.org/10.5194/acp-11-4289-2011>, 2011.

572 Gettelman, A., Morrison, H., Terai, C. R., and Wood, R.: Microphysical process rates and global

573 aerosolecloud interactions, *Atmos. Chem. Phys.*, 13, 9855–9867,

574 <https://doi.org/10.5194/acp-14-9099-2014>, 2013.

575 Han, H., Wu, Y., Liu, J., Zhao, T. L., Zhuang, B. L., Wang, H. L., Li, Y. C., Chen, H. M., Zhu, Y., Liu, H.

576 N., Wang, Q. G., Li, S., Wang, T. J., Xie, M., and Li, M. M.: Impacts of atmospheric transport and

577 biomass burning on the inter-annual variation in black carbon aerosols over the Tibetan Plateau,

578 *Atmos. Chem. Phys.*, 20, 13591–13610, <https://doi.org/10.5194/acp-20-13591-2020>, 2020.

579 [Healy, R. M., Sciare, J., Poulain, L., Crippa, M., Wiedensohler, A., Prévôt, A.S.H., Baltensperger, U.,](#)

580 [Sarda-Estève, R., McGuire, M. L., Jeong, C. H., McGillicuddy, E., O’Connor, I. P., Sodeau, J. R.,](#)

581 [Evans, G. J., and Wenger, J. C.: Quantitative determination of carbonaceous particle mixing state in](#)

582 [Paris using single-particle mass spectrometer and aerosol mass spectrometer measurements, *Atmos.*](#)

583 [*Chem. Phys.*, 13, 9479–9496, <http://dx.doi.org/10.5194/acp-13-9479-2013>, 2013.](#)

584 Hua, S., Liu, Y. Z., Luo, R., Shao, T. B., Zhu, Q. Z.: Inconsistent aerosol indirect effects on water clouds

585 and ice clouds over the Tibetan Plateau, *Int. J. Climatol.*, 40, 3832–3848,

586 <https://doi.org/10.1002/joc.6430>, 2019.

587 [Huang, X. J., Zhang, J. K., Luo, B., Luo, J. Q., Zhang, W., and Rao, Z. H.: Characterization of oxalic](#)

588 [acid-containing particles in summer and winter seasons in Chengdu, China, *Atmos. Environ.*, 198,](#)

589 [133–141. <https://doi.org/10.1016/j.atmosenv.2018.10.050>, 2019.](https://doi.org/10.1016/j.atmosenv.2018.10.050)

590 Immerzeel, W. W., van Beek, L. P. H., and Bierkens, M. F. P.: Climate change will affect the Asian water

591 towers, *Science*, 328, 1382–1385, <https://doi.org/10.1126/science.1183188>, 2010.

592 Jacobson, M. Z.: Analysis of aerosol interactions with numerical techniques for solving coagulation,

593 nucleation, condensation, dissolution, and reversible chemistry among multiple size distributions, *J.*

删除[Li]: Dusek, U., Frank, G. P., Hildebrandt, L., Curtius, J., Schneider, J., Walter, S., Chand, D., Drewnick, F., Hings, S., Jung, D., Borrmann, S., and Andreae, M. O.: Size matters more than chemistry for cloud-nucleating ability of aerosol particles, *Science*, 312, 1375–1378, <https://doi.org/10.1126/science.1125261>, 2006.

设置格式[Li]: 字体颜色: 自动设置

设置格式[Li]: 字体颜色: 自动设置

设置格式[Li]: 字体颜色: 自动设置

设置格式[Li]: 字体颜色: 自动设置

设置格式[Li]: 字体: (默认)Times New Roman, 字体颜色: 自动设置

设置格式[Li]: 字体: (默认)Times New Roman, 字体颜色: 自动设置

594 Geophys. Res., 107(D19), 4366, <https://doi.org/10.1029/2001JD002044>, 2002.

595 Jiang, H. H., Frie, A. L., Lavi, A., Chen, J. Y., Zhang, H., Bahreini, R., and Lin, Y. H.: Brown carbon
596 formation from nighttime chemistry of unsaturated heterocyclic volatile organic compounds, Environ.
597 Sci. Technol. Lett., 6, 184190, <https://doi.org/10.1021/acs.estlett.9b00017>, 2019.

598 [Kumar, M., Raju, M. P., Singh, R. K., Singh, A. K., Singh, R. S., and Banerjee, T.: Wintertime](#)
599 [characteristics of aerosols over middle Indo-Gangetic Plain: vertical profile, transport and radiative](#)
600 [forcing, Atmos. Res., 183, 268–282, <https://doi.org/10.1016/j.atmosres.2016.09.012>, 2017.](#)

601 [Kundu, S., Kawamura, K., Andreae, T. W., Hoffer, A., and Andreae, M. O.: Molecular distributions of](#)
602 [dicarboxylic acids, ketocarboxylic acids and alpha-dicarbonyls in biomass burning aerosols:](#)
603 [implications for photochemical production and degradation in smoke layers, Atmos. Chem. Phys., 10](#)
604 [\(5\), 2209–2225, <https://doi.org/10.5194/acp-10-2209-2010>, 2010.](#)

605 Lian, X. F., Zhang, G. H., Yang, Y. X., Lin, Q. H., Fu, Y. Z., Jiang, F., Peng, L., Hu, X. D., Chen, D. H.,
606 Wang, X. M., Peng, P. A., Sheng, G. Y., and Bi, X. H.: Evidence for the Formation of Imidazole from
607 Carbonyls and Reduced Nitrogen Species at the Individual Particle Level in the Ambient Atmosphere,
608 Environ. Sci. Technol. Lett., 8, 9–15. <https://dx.doi.org/10.1021/acs.estlett.0c00722>, 2021.

609 Liang, Z. C., Zhou, L. Y., Cuevas, R. A., Li, X. Y., Cheng, C. L., Li, M., Tang, R. Z., Zhang, R. F., Lee
610 Patrick K. H., Lai, Alvin C. K., and Chan, C.K.: Sulfate Formation in Incense Burning Particles: A
611 Single-Particle Mass Spectrometric Study, Environ. Sci. Technol. Lett., 9, 718–725,
612 <https://doi.org/10.1021/acs.estlett.2c00492>, 2022.

613 Li, C. L., Bosch, C., Kang, S. C., Andersson, A., Chen, P. F., Zhang, Q. G., Cong, Z. Y., Chen, B., Qin, D.
614 H., and Gustafsson, Ö.: Sources of black carbon to the Himalayan–Tibetan Plateau glaciers, Nat.
615 Commun., 7, 12574, <https://doi.org/10.1038/ncomms12574>, 2016b.

616 Li, C. L., Bosch, C., Kang, S. C., Andersson, A., Chen, P. F., Zhang, Q. G., Cong, Z. Y., Tripathee, L., and
617 Örtjanb, G.: ¹⁴C characteristics of organic carbon in the atmosphere and at glacier region of the Tibetan
618 Plateau, Sci. Total Environ., 832, 155020, <https://doi.org/10.1016/j.scitotenv.2022.155020>, 2022a.

619 [Li, L., Huang, Z. X., Dong, J. G., Li, M., Gao, W., Nian, H. Q., Fu, Z., Zhang, G. H., Bi, X. H., Cheng, P.,](#)
620 [and Zhou, Z.: Real time bipolar time-of-flight mass spectrometer for analyzing single aerosol particles,](#)
621 [Int. J. Mass Spectrom., 303, 118–124, <https://doi.org/10.1016/j.ijms.2011.01.017>, 2011.](#)

622 [Li L., Wang, Q. Y., Zhang, Y., Liu, S. X., Zhang, T., Wang, S., Tian, J., Chen, Y., Hang Ho, S. S., Han, Y.,](#)
623 [and Cao, J.J.: Impact of reduced anthropogenic emissions on chemical characteristics of urban aerosol](#)
624 [by individual particle analysis, Chemosphere, 303, 135013,](#)
625 [https://doi.org/10.1016/j.chemosphere.2022.135013, 2022b.](#)

626 [Li, J. J., Wang, G. H., Wang, X. M., Cao, J. J., Sun, T., Cheng, C. L., Meng, J. J., Hu, T. F., and Liu, S. X.:](#)
627 [Abundance, composition and source of atmospheric PM_{2.5} at a remote site in the Tibetan Plateau,](#)
628 [China, Tellus B, 65, <http://dx.doi.org/10.3402/tellusb.v65i0.20281>, 2013.](#)

629 Li, Y. J., Sun, Y. L., Zhang, Q., Li, X., Li, M., Zhou, Z., and Chan, C. K.: Real-time chemical
630 characterization of atmospheric particulate matter in China: A review, Atmos. Environ., 158, 270–304,
631 <http://dx.doi.org/10.1016/j.atmosenv.2017.02.027>, 2017.

632 [Lin, Q. H., Bi, X. H., Zhang, G. H., Yang, Y. X., Peng, L., Lian, X. F., Fu, Y. Z., Li, M., Chen, D. H., Miller,](#)
633 [M., Ou, J., Tang, M. J., Wang, X. M., Peng, P. A., Sheng, G. Y., and Zhou, Z.: In-cloud formation of](#)
634 [secondary species in iron-containing particles, Atmos. Chem. Phys., 19, 1195–1206,](#)
635 [https://doi.org/10.5194/acp-19-1195-2019, 2019](#)

636 Link, M. F., Kim, J., Park, G., Lee, T., Park, T., Babar, Z. B., Sung, K., Kim, P., Kang, S., Kim, J. S., Choi,
637 Y., Son, J., Lim, H. J., and Farmer, D.K.: Elevated production of NH₄NO₃ from the photochemical

删除[Li]: Kawamura, K. and Bikkina, S.: A review of dicarboxylic acids and related compounds in atmospheric aerosols: molecular distributions, sources and transformation, Atmos. Res., 170, 140–160, <https://doi.org/10.1016/j.atmosres.2015.11.018>, 2016.

设置格式[Li]: 字体颜色: 自动设置

设置格式[Li]: 字体颜色: 自动设置

设置格式[Li]: 字体颜色: 自动设置

删除[Li]: Li, L., Li, M., Huang, Z. X., Gao, W., Nian, H. Q., Fu, Z., Gao, J., Chai, F. H., and Zhou, Z.: Ambient particle characterization by single particle aerosol mass spectrometry in an urban area of Beijing, Atmos. Environ., 94, 323–331, <https://doi.org/10.1016/j.atmosenv.2014.03.048>, 2014.

设置格式[Li]: 字体颜色: 自动设置

设置格式[Li]: 字体颜色: 自动设置

设置格式[Li]: 字体颜色: 自动设置

设置格式[Li]: 字体颜色: 自动设置

设置格式[Li]: 字体颜色: 自动设置

638 processing of vehicle exhaust: Implications for air quality in the Seoul Metropolitan Region, *Atmos.*
639 *Environ.*, 156, 95–101, <https://doi.org/10.1016/j.atmosenv.2017.02.031>, 2017.

640 Liu, Y. Z., Zhu, Q. Z., Huang, J. P., Hua, S., and Jia, R.: Impact of dust-polluted convective clouds over the
641 Tibetan Plateau on downstream precipitation, *Atmos. Environ.*, 209, 67–77,
642 <https://doi.org/10.1016/j.atmosenv.2019.04.001>, 2019.

643 Liu, Q., Liu, D. T., Gao, Q., Tian, P., Wang, F., Zhao, D. L., Bi, K., Wu, Y. Z., Ding, S., Hu, K., Zhang, J.
644 L., Ding, D. P., [and](#) Zhao, C. S.: Vertical characteristics of aerosol hygroscopicity and impacts on
645 optical properties over the North China Plain during winter, *Atmos. Chem. Phys.*, 20, 3931–3944,
646 <https://doi.org/10.5194/acp-20-3931-2020>, 2020a.

647 Liu, D. T., Hu, K., Zhao, D. L., Ding, S., Wu, Y. F., Zhou, C., Yu, C. J., Tian, P., Liu, Q., Bi, K., Wu, Y. Z.,
648 Hu, B., Ji, D. S., Kong, S. F., Ouyang, B., He, H., Huang, M. Y., and Ding, D.P.: Efficient Vertical
649 Transport of Black Carbon in the Planetary Boundary Layer, *Geo. Res. Lett.*, 47, 1–10, <https://doi.org/10.1029/2020GL088858>, 2020b

651 Liu, H. K., Wang, Q. Y., Xing, L., Zhang, Y., Zhang, T., Ran, W. K., [and](#) Cao, J. J.: Measurement report:
652 quantifying source contribution of fossil fuels and biomass-burning black carbon aerosol in the
653 southeastern margin of the Tibetan Plateau, *Atmos. Chem. Phys.*, 21, 973–987,
654 <https://doi.org/10.5194/acp-21-973-2021>, 2021.

655 [Liu, X. D., Dong, B. W., Yin, Z. Y., Smith, R. S., Guo, Q. C.: Continental drift and plateau uplift control](#)
656 [origination and evolution of Asian and Australian monsoons, *Sci. Rep.*, 7, 40344, <https://doi.org/10.1038/srep40344>, 2017.](#)

658 Luo, M., Liu, Y. Z., Zhu, Q. Z., Tang, Y. H., and Alam, K.: Role and mechanisms of black carbon affecting
659 water vapor transport to Tibet, *Remote Sens.*, 12, 231, <https://doi.org/10.3390/rs12020231>, 2020.

660 Ma, L., Li, M., Huang, Z. X., Li, L., Gao, W., Nian, H. Q., Zou, L. L., Fu, Z., Gao, J., Chai, F. H., and
661 Zhou, Z.: Real time analysis of lead-containing atmospheric particles in Beijing during springtime by
662 single particle aerosol mass spectrometry, *Chemosphere*, 154, 454–462,
663 <https://doi.org/10.1016/j.chemosphere.2016.04.001>, 2016.

664 Ma, X., Yu, F., and Luo, G.: Aerosol direct radiative forcing based on GEOS-Chem-APM and uncertainties,
665 *Atmos. Chem. Phys.*, 12, 5563–5581, <https://doi.org/10.5194/acp-12-5563-2012>, 2012.

666 [Matsui, H.: Black carbon simulations using a size- and mixingstate-resolved three-dimensional model: 2.](#)
667 [Aging timescale and its impact over East Asia, *J. Geophys. Res.-Atmos.*, 121, 1808–1821,](#)
668 [https://doi.org/10.1002/2015jd023999, 2016.](#)

669 [Meng, J. J., Wang, G. H., Li, J. J., Cheng, C. L., Ren, Y. Q., Huang, Y., Cheng, Y. T., Cao, J. J., and Zhang, T.:](#)
670 [Seasonal characteristics of oxalic acid and related SOA in the free troposphere of Mt. Hua, central](#)
671 [China: implications for sources and formation mechanisms, *Sci. Total Environ.*, 493, 1088–1097,](#)
672 [https://doi.org/10.1016/j.scitotenv.2014.04.086, 2014.](#)

673 [Meng, J. J., Liu, X. D., Hou, Z. F., Yi, Y. N., Yan, L., Li, Z., Cao, J.J., Li, J. J., Wang, G. H.: Molecular](#)
674 [characteristics and stable carbon isotope compositions of dicarboxylic acids and related compounds in](#)
675 [the urban atmosphere of the North China Plain: implications for aqueous phase formation of SOA](#)
676 [during the haze periods, *Sci. Total Environ.*, 705, 135256,](#)
677 [https://doi.org/10.1016/j.scitotenv.2019.135256, 2020.](#)

678 [Ng, N. L., Canagaratna, M. R., Jimenez, J. L., Chhabra, P. S., Seinfeld, J. H., and Worsnop, D. R.: Changes](#)
679 [in organic aerosol composition with aging inferred from aerosol mass spectra, *Atmos. Chem. Phys.*,](#)
680 [11\(13\), 6465–6474, <https://doi.org/10.5194/acp-11-6465-2011>, 2011.](#)

681 [Peng, J. F., Hu, M., Guo, S., Du, Z. F., Zheng, J., Shang, D. J., Zamora, M. L., Zeng, L. M., Shao, M., Wu,](#)

设置格式[Li]: 字体颜色: 自动设置

删除[Li]: Mahowald, N. M., Albani, S., Kok, J. F., Engelstaedter, S., Scanza, R., Ward, D. S., and Flanner, M. G.: The size distribution of desert dust aerosols and its impact on the Earth system, *Aeolian Res.*, 15, 53–71, <https://doi.org/10.1016/j.aeolia.2013.09.002>, 2014.

删除[Li]: McFiggans, G., Artaxo, P., Baltensperger, U., Coe, H., Facchini, M.C., Feingold, G., Fuzzi, S., Gysel, M., Laaksonen, A., Lohmann, U., Mentel, T. F., Murphy, D. M., O’Dowd, C. D., Snider, J.R., and Weingartner, E.: The effect of physical and chemical aerosol properties on warm cloud droplet activation, *Atmos. Chem. Phys.*, 6, 2593–2649, <https://doi.org/10.5194/acp-6-2593-2006>, 2006.

Moffet, R. C., Foy, B. D., Molina, L. A., Molina, M. J., and Prather, K. A.: Measurement of ambient aerosols in northern Mexico City by single particle mass spectrometry, *Atmos. Chem. Phys.*, 8 (16), 4499–4516, <https://doi.org/10.5194/acpd-7-6413-2007>, 2008.

设置格式[Li]: 字体颜色: 自动设置

删除[Li]: Nie, W., Wang, T., Xue, L. K., and Ding, A. J.: Asian dust storm observed at a rural mountain site in southern china: chemical evolution and heterogeneous photochemistry, *Atmos. Chem. Phys.*, 12, 11985–11995, <https://doi.org/10.5194/acp-12-11985-2012>, 2012.

682 [Y. S., Zheng, J., Wang, Y., Glen, C. R., Collins, D. R., Molina, M. J., and Zhang, R. Y.: Markedly](#)
683 [enhanced absorption and direct radiative forcing of black carbon under polluted urban environments,](#)
684 [P. Natl. Acad. Sci. USA, 113, 4266–4271, https://doi.org/10.1073/pnas.1602310113, 2016.](#)

685 Pratt, K. A., Hatch, L. E., and Prather, K. A.: Seasonal volatility dependence of ambient particle phase
686 amines, *Environ. Sci. Technol.*, 43, 5276–5281, <https://doi.org/10.1021/es803189n>, 2009.

687 [Pratt, K. A., Murphy, S. M., Subramanian, R., DeMott, P. J., Kok, G. L., Campos, T., Rogers, D. C., Prenni,](#)
688 [A. J., Heymsfield, A. J., Seinfeld, J. H., and Prather, K. A.: Flight-based chemical characterization of](#)
689 [biomass burning aerosols within two prescribed burn smoke plumes, *Atmos. Chem. Phys.*, 11,](#)
690 [12549–12565, https://doi.org/10.5194/acp-11-12549-2011, 2011.](#)

691 [Qian, Y., Flanner, M. G., Leung, L. R., and Wang, W.: Sensitivity studies on the impacts of Tibetan Plateau](#)
692 [snowpack pollution on the Asian hydrological cycle and monsoon climate, *Atmos. Chem. Phys.*, 11,](#)
693 [1929–1948, https://doi.org/10.5194/acp-11-1929-2011, 2011.](#)

694 [Rehbein, P. J., Jeong, C. H., McGuire, M. L., Yao, X., Corbin, J. C., and Evans, G. J.: Cloud and fog](#)
695 [processing enhanced gas-to-particle partitioning of trimethylamine, *Environ. Sci. Technol.*, 45,](#)
696 [4346–4352, https://doi.org/10.1021/es1042113, 2011.](#)

697 [Roth, A., Schneider, J., Klimach, T., Mertes, S., van Pinxteren, D., Herrmann, H., and Borrmann, S.:](#)
698 [Aerosol properties, source identification, and cloud processing in orographic clouds measured by](#)
699 [single particle mass spectrometry on a central European mountain site during HCCT-2010, *Atmos.*](#)
700 [*Chem. Phys.*, 16, 505–524, https://doi.org/10.5194/acp-16-505-2016, 2016.](#)

701 [Shen, L. J., Wang, H. L., Yin, Y., Chen, J. H., and Chen, K.: Observation of atmospheric new particle](#)
702 [growth events at the summit of mountain Tai \(1534 m\) in Central East China, *Atmos. Environ.*, 201,](#)
703 [148–157, https://doi.org/10.1016/j.atmosenv.2018.12.051, 2019.](#)

704 Shen, L. J., Wang, H. L., Lü, S., Zhang, X. H., Yuan, J., Tao, S. K., Zhang, G. J., Wang, F., and Li, L.:
705 Influence of pollution control on air pollutants and the mixing state of aerosol particles during the 2nd
706 World Internet Conference in Jiaying, China, *J. Clean. Prod.*, 149, 436–447,
707 <https://doi.org/10.1016/j.jclepro.2017.02.114>, 2017.

708 Shen, R. Q., Ding, X., He, Q. F., Cong, Z. Y., Yu, Q. Q., and Wang, X. M.: Seasonal variation of secondary
709 organic aerosol tracers in Central Tibetan Plateau, *Atmos. Chem. Phys.*, 15, 8781–8793,
710 <https://doi.org/10.5194/acp-15-8781-2015>, 2015.

711 Sirois, A. and Bottenheim, J. W.: Use of backward trajectories to interpret the 5-year record of PAN and O₃
712 ambient air concentrations at Kejimikujik National Park, Nova Scotia, *J. Geophys. Res.*, 100,
713 2867–2881, <https://doi.org/10.1029/94JD02951>, 1995.

714 Song, X. H., and Hopke, P. K.: Classification of single particles analyzed by ATOFMS using an artificial
715 neural network, *ART-2A, Anal. Chem.*, 71, 860–865, <https://doi.org/10.1021/ac9809682>, 1999.

716 Sorooshian, A., Lu, M. L., Brechtel, F. J., Jonsson, H., Feingold, G., Flagan, R. C., and Seinfeld, J. H.: On
717 the source of organic acid aerosol layers above clouds, *Environ. Sci. Technol.*, 41, 4647–4654,
718 <https://doi.org/10.1021/es0630442>, 2007.

719 Sullivan, R. C., Guazzotti, S. A., Sodeman, D. A., and Prather, K. A.: Direct observations of the
720 atmospheric processing of Asian mineral dust, *Atmos. Chem. Phys.*, 7, 1213–1236,
721 <https://doi.org/10.5194/acp-7-1213-2007>, 2007.

722 Sun, Y. L., Wang, Z. F., Fu, P. Q., Jiang, Q. J., Yang, T., Li, J., and Ge, X. L.: The impact of relative
723 humidity on aerosol composition and evolution processes during wintertime in Beijing, China, *Atmos.*
724 *Environ.*, 77, 927–934, <https://doi.org/10.1016/j.atmosenv.2013.06.019>, 2013.

725 [Tian, J., Wang, Q. Y., Zhang, Y., Yan, M. Y., Liu, H. K., Zhang, N. N., Ran, W. K., and Cao, J. J.: Impacts](#)

设置格式[Li]: 字体颜色: 自动设置

设置格式[Li]: 字体颜色: 自动设置

删除[Li]: Pratt, K.A. and Prather, K.A.: Aircraft
measurements of vertical profiles of aerosol mixing states, *J.*
Geophys. Res., 115, D11305,
<https://doi.org/10.1029/2009jd013150>, 2010.

Prather, P.A., Nordmeyer, T., and Salt, K.: Real-time
characterization of individual aerosol particles using
time-of-flight mass spectrometry, *Anal. Chem.*, 66, 1403–1407,
<https://dx.doi.org/10.1021/ac00081a007>, 1994.

设置格式[Li]: 字体颜色: 自动设置

设置格式[Li]: 字体颜色: 自动设置

设置格式[Li]: 字体颜色: 自动设置

删除[Li]: Robinson, A. L., Donahue, N. M., Shrivastava, M.
K., Weitkamp, E. A., Sage, A. M., Grieshop, A. P., Lane, T. E.,
Pierce, J. R., and Pandis, S.N.: Rethinking organic aerosols:
Semivolatile emissions and photochemical aging, *Science*, 315,
1259–1262, <https://doi.org/10.1126/science.1133061>, 2007.

删除[Li]: Seinfeld, J. H., and Pandis, S. N.: *Atmospheric*
Chemistry and Physics: from Air Pollution to Climate Change,
John Wiley & Sons., 1326.
<https://doi.org/10.1080/00139157.1999.10544295>, 2012.

设置格式[Li]: 字体颜色: 自动设置

设置格式[Li]: 字体颜色: 自动设置

设置格式[Li]: 字体颜色: 自动设置

设置格式[Li]: 字体: (默认)Times New Roman, 字体颜色:
自动设置

726 [of primary emissions and secondary aerosol formation on air pollution in an urban area of China](#)
727 [during the COVID-19 lockdown, Environ. Int., 150, 106426–14,](#)
728 <https://doi.org/10.1016/j.envint.2021.106426>, 2021.

729 Wang, A. Q., Xie, X. N., Liu, X. D., and Yin, Z. Y.: Direct Radiative Effect (DRE) of Dust Aerosols on
730 West African and East Asian Monsoon: The Role of Ocean-Atmosphere Interactions, *J. Geophys.*
731 *Res. Atmos.*, 127, 1–20, <https://doi.org/10.1029/2021JD035917>, 2022.

732 Wang, G. H., Zhang, R. Y., Gomez, M. E., Yang, L. X., Zamora, M. L., Hu, M., Lin, Y., Peng, J. F., Guo, S.,
733 Meng, J. J., Li, J. J., Cheng, C. L., Hu, T. F., Ren, Y. Q., Wang, Y. S., Gao, J., Cao, J. J., An, Z. S.,
734 Zhou, W. J., Li, G. H., Wang, J. Y., Tian, P. F., Marrero-Ortiz, W., Secrest, J., Du, Z. F., Zheng, J.,
735 Shang, D. J., Zeng, L. M., Shao, M., Wang, W. G., Huang, Y., Wang, Y., Zhu, Y. J., Li, Y. X., Hu, J. X.,
736 Pan, B. W., Cai, L., Cheng, Y. T., Ji, Y. M., Zhang, Y., Rosenfeld, D., Liss, P. S., Duce, R. A., Kolb, C.
737 E., and Molina, M. J.: Persistent sulfate formation from London Fog to Chinese haze, *P. Natl. Acad.*
738 *Sci. USA*, 113(48), 13630–13635, <https://doi.org/10.1073/pnas.1616540113>, 2016.

739 Wang, H. C., Lu, K. D., Chen, X. R., Zhu, Q. D., Chen, Q., Guo, S., Jiang, M. Q., Li, X., Shang, D. J., Tan,
740 Z. F., Wu, Y. S., Wu, Z. J., Zou, Q., Zheng, Y., Zeng, L. M., Zhu, T., Hu, M., Zhang, Y. H.: High
741 N₂O₅ concentrations observed in urban Beijing: implications of a large nitrate formation pathway,
742 *Environ. Sci. Technol. Lett.*, 4, 416–420, <https://doi.org/10.1021/acs.estlett.7b00341>, 2017.

743 Wang, H. L., An, J. L., Shen, L. J., Zhu, B., Xia, L., Duan, Q., and Zou, J. N.: Mixing state of ambient
744 aerosols in Nanjing city by single particle mass spectrometry, *Atmos. Environ.*, 132, 123–132,
745 <https://dx.doi.org/10.1016/j.atmosenv.2016.02.032>, 2016.

746 Wang, Q. Y., Han, Y. M., Ye, J. H., Liu, S. X., Pongpiachan, S., Zhang, N. N., Han, Y. M., Tian, J., Wu, C.,
747 Long, X., Zhang, Q., Zhang, W. Y., Zhao, Z. Z., and Cao, J. J.: High contribution of secondary brown
748 carbon to aerosol light absorption in the southeastern margin of Tibetan Plateau, *Geophys. Res. Lett.*,
749 46, 4962–4970, <https://doi.org/10.1029/2019GL082731>, 2019a.

750 Wang, H. L., Shen, L. J., Yin, Y., Chen, K., Chen, J. H., and Wang, Y. S.: Characteristics and mixing state
751 of aerosol at the summit of Mount Tai (1534 m) in Central East China: First measurements with
752 SPAMS, *Atmos. Environ.*, 213, 273–284, <https://doi.org/10.1016/j.atmosenv.2019.06.021>, 2019b.

753 Wang, Q. Y., Cao, J. J., Han, Y. M., Tian, J., Zhu, C. S., Zhang, Y., Zhang, N. N., Shen, Z. X., Ni, H. Y.,
754 Zhao, S. Y., and Wu, J. R.: Sources and physicochemical characteristics of black carbon aerosol from
755 the southeastern Tibetan Plateau: internal mixing enhances light absorption, *Atmos. Chem. Phys.*, 18,
756 4639–4656, <https://doi.org/10.5194/acp-18-4639-2018>, 2018.

757 Wenzel, R. J., Liu, D.-Y., Edgerton, E. S., and Prather, K. A.: Aerosol time-of-flight mass spectrometry
758 during the Atlanta Supersite Experiment: 2. Scaling procedures, *J. Geophys. Res.*, 108, 8427,
759 <http://dx.doi.org/10.1029/2001jd001563>, 2003.

760 Wood, E. C., Canagaratna, M. R., Herndon, S. C., Onasch, T. B., Kolb, C. E., Worsnop, D. R., Kroll, J. H.,
761 Knighton, W. B., Seila, R., Zavala, M., Molina, L. T., DeCarlo, P. F., Jimenez, J. L., Weinheimer, A. J.,
762 Knapp, D. J., Jobson, B. T., Stutz, J., Kuster, W. C., and Williams, E. J.: Investigation of the
763 correlation between odd oxygen and secondary organic aerosol in Mexico City and Houston, *Atmos.*
764 *Chem. Phys.*, 10, 8947–8968, <https://doi.org/10.5194/acp-10-8947-2010>, 2010.

765 Xu, L. L., Wu, X., Hong, Z. Y., Zhang, Y. R., Deng, J. J., Hong, Y. W., and Chen, J. S.: Composition,
766 mixing state, and size distribution of single submicron particles during pollution episodes in a coastal
767 city in southeast China, *Environ. Sci. Pollut. Res.*, 26, 1464–1473,
768 <https://doi.org/10.1007/s11356-018-3469-x>, 2018.

769 Xu, W. Q., Han, T. T., Du, W., Wang, Q. Q., Chen, C., Zhao, J., Zhang, Y. J., Li, J., Fu, P. Q., Wang, Z. F.,

设置格式[Li]: 字体: (默认)Times New Roman, 字体颜色: 自动设置

删除[Li]: Volkamer, R., Jimenez, J. L., San Martini, F., Dzepina, K., Zhang, Q., Salcedo, D., Molina, L. T., Worsnop, D. R., and Molina, M. J.: Secondary organic aerosol formation from anthropogenic air pollution: rapid and higher than expected, *Geophys. Res. Lett.*, 33 (17), <https://doi.org/10.1029/2006GL026899>, 2006.

设置格式[Li]: 字体颜色: 自动设置

设置格式[Li]: 字体颜色: 自动设置

删除[Li]: William, K.M.L., Maeng-Ki, K., Kyu-Myong, K., and Woo-Seop, L.: Enhanced surface warming and accelerated snow melt in the Himalayas and Tibetan Plateau induced by absorbing aerosols, *Environ. Res. Lett.*, 5(2), 025204, <https://doi.org/10.1088/1748-9326/5/2/025204>, 2010.

删除[Li]: Xia, X., Chen, H., Goloub, P., Zhang, W., Chatenet, B., and Wang, P.: A compilation of aerosol optical properties and calculation of direct radiative forcing over an urban region in northern China, *J. Geophys. Res.*, 112, D12203, <https://doi.org/10.1029/2006jd008119>, 2007.

770 Worsnop, D. R., and Sun, Y. L.: Effects of aqueous-phase and photochemical processing on secondary
771 organic aerosol formation and evolution in Beijing, China, *Environ. Sci. Technol.*, 51, 762–770,
772 <https://doi.org/10.1021/acs.est.6b04498>, 2017.

773 Xue, J., Griffith, S. M., Yu, X., Lau, A.K.H., and Yu, J. Z.: Effect of nitrate and sulfate relative abundance
774 in PM_{2.5} on liquid water content explored through half-hourly observations of inorganic soluble
775 aerosols at a polluted receptor site, *Atmos. Environ.*, 99, 24–31,
776 <https://doi.org/10.1016/j.atmosenv.2014.09.049>, 2014.

777 Yang, J., Ma, S. X., Gao, B., Li, X. Y., Zhang, Y. J., Cai, J., Li, M., Yao, L. A., Huang, B., and Zheng, M.:
778 Single particle mass spectral signatures from vehicle exhaust particles and the source apportionment
779 of on-line PM_{2.5} by single particle aerosol mass spectrometry, *Sci. Total Environ.*, 593, 310–318,
780 <https://doi.org/10.1016/j.scitotenv.2017.03.099>, 2017.

781 [Zauscher, M. D., Wang, Y., Moore, M. J. K., Gaston, C. J., and Prather, K. A.: Air Quality Impact and](#)
782 [Physicochemical Aging of Biomass Burning Aerosols during the 2007 San Diego Wildfires, *Environ.*](#)
783 [*Sci. Technol.*, 47, 7633–7643, <https://doi.org/10.1021/es4004137>, 2013.](#)

784 Zaveri, R. A., Barnard, J., Easter, R., Riemer, N., and West, M.: Particle-resolved simulation of aerosol size,
785 composition, mixing state, and the associated optical and cloud condensation nuclei activation
786 properties in an evolving urban plume, *J. Geophys. Res.*, 115, D17210,
787 <https://doi.org/10.1029/2009JD013616>, 2010.

788 Zhang, G. H., Bi, X. H., Chan, L. Y., Li, L., Wang, X. M., Feng, J. L., Sheng, G. Y., Fu, J. M., Li, M., and
789 Zhou, Z.: Enhanced trimethylamine-containing particles during fog events detected by single particle
790 aerosol mass spectrometry in urban Guangzhou, China, *Atmos. Environ.*, 55, 121–126,
791 <https://doi.org/10.1016/j.atmosenv.2012.03.038>, 2012.

792 Zhang, G. H., Han, B. X., Bi, X. H., Dai, S. X., Huang, W., Chen, D. H., Wang, X. M., Sheng, G. Y., Fu, J.
793 M., and Zhou, Z.: Characteristics of individual particles in the atmosphere of Guangzhou by single
794 particle mass spectrometry, *Atmos. Res.*, 153, 286–295,
795 <https://doi.org/10.1016/j.atmosres.2014.08.016>, 2015.

796 Zhang, J. K., Luo, B., Zhang, J. Q., Ouyang, F., Song, H. Y., Liu, P. C., Cao, P., Schäfer, K., Wang, S. G.,
797 Huang, X. J., and Lin, Y. F.: Analysis of the characteristics of single atmospheric particles in Chengdu
798 using single particle mass spectrometry, *Atmos. Environ.*, 157, 91–100,
799 <https://doi.org/10.1016/j.atmosenv.2017.03.012>, 2017a.

800 [Zhang, G. H., Lin, Q. H., Peng, L., Yang, Y. X., Fu, Y. Z., Bi, X. H., Li, M., Chen, D. H., Chen, J. X., Cai,](#)
801 [Z., Wang, X. M., Peng, P. A., Sheng, G. Y., Zhou, Z.: Insight into the in-cloud formation of oxalate](#)
802 [based on in situ measurement by single particle mass spectrometry, *Atmos. Chem. Phys.*, 17 \(22\),](#)
803 [13891–13901, <https://doi.org/10.5194/acp-17-13891-2017>, 2017b.](#)

804 Zhang, G. H., Han, B. X., Bi, X. H., Dai, S. X., Huang, W., Chen, D. H., Wang, X. M., Sheng, G. Y., Fu, J.
805 M., and Zhou, Z.: Characteristics of individual particles in the atmosphere of Guangzhou by single
806 particle mass spectrometry, *Atmos. Res.*, 153, 286–295,
807 <https://dx.doi.org/10.1016/j.atmosres.2014.08.016>, 2015.

808 [Zhang, G. H., Lian, X. F., Fu, Y. Z., Lin, Q. H., Li, L., Song, W., Wang, Z. Y., Tang, M. J., Chen, D. H., Bi,](#)
809 [X. H., Wang, X. M., and Sheng, G. Y.: High secondary formation of nitrogen-containing organics](#)
810 [\(NOCs\) and its possible link to oxidized organics and ammonium, *Atmos. Chem. Phys.*, 20,](#)
811 [1469–1481, <https://doi.org/10.5194/acp-20-1469-2020>, 2020.](#)

812 Zhang, X. H., Xu, J. Z., Kang, S. C., Zhang, Q., and Sun, J. Y.: Chemical characterization and sources of
813 submicron aerosols in the northeastern Qinghai–Tibet Plateau: insights from high-resolution mass

删除[Li]: Yao, T. D., Thompson, L. G., Mosbrugger, V., (中 ...)

设置格式[Li]: 字体: (默认) Times New Roman, (中 ...)

设置格式[Li]: 字体颜色: 自动设置

设置格式[Li]: 字体: (默认) Times New Roman, (中 ...)

设置格式[Li]: 字体颜色: 自动设置

设置格式[Li]: 字体: (默认) Times New Roman, (中 ...)

设置格式[Li]: 字体颜色: 自动设置

设置格式[Li]: 字体: (默认) Times New Roman, (中 ...)

设置格式[Li]: 字体颜色: 自动设置

设置格式[Li]: 字体: (默认) Times New Roman, (中 ...)

设置格式[Li]: 字体颜色: 自动设置

设置格式[Li]: 字体: (默认) Times New Roman, (中 ...)

设置格式[Li]: 字体颜色: 自动设置

设置格式[Li]: 字体: (默认) Times New Roman, (中 ...)

设置格式[Li]: 字体颜色: 自动设置

设置格式[Li]: 字体: (默认) Times New Roman, (中 ...)

设置格式[Li]: 字体颜色: 自动设置

设置格式[Li]: 字体: (默认) Times New Roman, (中 ...)

设置格式[Li]: 字体颜色: 自动设置

设置格式[Li]: 字体: (默认) Times New Roman, (中 ...)

设置格式[Li]: 字体颜色: 自动设置

设置格式[Li]: 字体: (默认) Times New Roman, (中 ...)

设置格式[Li]: 字体颜色: 自动设置

设置格式[Li]: 字体: (默认) Times New Roman, (中 ...)

设置格式[Li]: 字体颜色: 自动设置

设置格式[Li]: 字体: (默认) Times New Roman, (中 ...)

设置格式[Li]: 字体颜色: 自动设置

设置格式[Li]: 字体: (默认) Times New Roman, (中 ...)

设置格式[Li]: 字体颜色: 自动设置

设置格式[Li]: 字体: (默认) Times New Roman, (中 ...)

设置格式[Li]: 字体颜色: 自动设置

设置格式[Li]: 字体: (默认) Times New Roman, (中 ...)

设置格式[Li]: 字体颜色: 自动设置

设置格式[Li]: 字体: (默认) Times New Roman, (中 ...)

814 spectrometry, *Atmos. Chem. Phys.*, 19, 7897–7911, <https://doi.org/10.5194/acp-19-7897-2019>, 2019a.
815 [Zhang, G. H., Lin, Q. H., Peng, L., Yang, Y. X., Jiang, F., Liu, F. X., Song, W., Chen, D. H., Cai, Z., Bi, X.](#)
816 [H., Miller, M., Tang, M. J., Huang, W. L., Wang, X. M., Peng, P. A., Shen, G. Y.: Oxalate Formation](#)
817 [Enhanced by Fe-Containing Particles and Environmental Implications, *Environ. Sci. Technol.*, 53,](#)
818 [1269–1277, <https://doi.org/10.1021/acs.est.8b05280>, 2019b.](#)
819 Zhang, N. N., Cao, J. J., Xu, H. M., and Zhu, C. S.: Elemental compositions of PM_{2.5} and TSP in Lijiang,
820 southeastern edge of Tibetan Plateau during pre-monsoon period, *Particuology*, 11(1), 63–69,
821 <https://doi.org/10.1016/j.partic.2012.08.002>, 2013.
822 Zhang, S. P., Xing, J., Sarwar, G., Ge, Y. L., He, H., Duan, F. K., Zhao, Y., He, K. B., Zhu, L. D., Chu, B.
823 W.: Parameterization of heterogeneous reaction of SO₂ to sulfate on dust with coexistence of NH₃ and
824 NO₂ under different humidity conditions, *Atmos. Environ.*, 208, 133–140,
825 <https://doi.org/10.1016/j.atmosenv.2019.04.004>, 2019c.
826 [Zhao, S. Y., Tie, X. X., Long, X., and Cao, J. J.: Impacts of Himalayas on black carbon over the Tibetan](#)
827 [Plateau during summer monsoon, *Sci. Total Environ.*, 598, 307–318,](#)
828 <https://doi.org/10.1016/j.scitotenv.2017.04.101>, 2017.
829

设置格式[Li]: 字体颜色: 自动设置

设置格式[Li]: 字体颜色: 自动设置

设置格式[Li]: 字体颜色: 自动设置

设置格式[Li]: 超链接, 字体: (默认) Times New Roman,
无下划线, 字体颜色: 自动设置

设置格式[Li]: 超链接, 字体: (默认) Times New Roman,
无下划线, 字体颜色: 自动设置

设置格式[Li]: 超链接, 字体: (默认) Times New Roman,
无下划线, 字体颜色: 自动设置

设置格式[Li]: 超链接, 字体: (默认) Times New Roman,
无下划线, 字体颜色: 自动设置

设置格式[Li]: 字体颜色: 自动设置

删除[Li]: b

设置格式[Li]: 字体颜色: 自动设置

删除[Li]: Zhu, C. S., Cao, J. J., Hu, T. F., Shen, Z. X., Tie, X.
X., Huang, H., Wang, Q. Y., Huang, R. J., Zhao, Z. Z., Mocnik,
G., and Hansen, A.D.A.: Spectral dependence of aerosol light
absorption at an urban and a remote site over the Tibetan
Plateau, *Sci. Total Environ.*, 591, 14–21,
<https://doi.org/10.1016/j.scitotenv.2017.03.057>, 2017.

830 Table 1. The number concentrations, average percentages and characteristic ions of nine types
 831 of particles during the entire study period, and the average percentages of the major six
 832 particle types during two episodes.

Type	Number count	Fraction in total (%)	Episode 1 (%)	Episode 2 (%)	Tracer ions
rich-K	151040	30.9	29.0	39.3	$^{39}\text{K}^+$, $^{26}\text{CN}^-$, $^{42}\text{CNO}^-$, $^{46}\text{NO}_2^-$, $^{62}\text{NO}_3^-$, $^{97}\text{HSO}_4^-$
BB	91322	18.7	11.5	14.2	$^{39}\text{K}^+$, levoglucosan ($^{45}\text{CHO}_2^-$, $^{59}\text{C}_2\text{H}_3\text{O}_2^-$, $^{71}\text{C}_3\text{H}_3\text{O}_2^-$, $^{73}\text{C}_3\text{HO}_3^-$), $^{26}\text{CN}^-$, $^{35,37}\text{Cl}^-$, $^{42}\text{CNO}^-$, $^{46}\text{NO}_2^-$, $^{62}\text{NO}_3^-$, $^{97}\text{HSO}_4^-$
OC	62446	12.8	8.1	10.0	$^{27}\text{C}_2\text{H}_3^+$, $^{37}\text{C}_3\text{H}^+$, $^{38}\text{C}_3\text{H}_2^+$, $^{39}\text{K}^+/\text{C}_3\text{H}_3^+$, $^{43}\text{C}_2\text{H}_3\text{O}^+$, $^{51}\text{C}_4\text{H}_3^+$, $^{26}\text{CN}^-$, $^{42}\text{CNO}^-$, $^{46}\text{NO}_2^-$, $^{62}\text{NO}_3^-$, $^{97}\text{HSO}_4^-$
Ammonium	58317	11.9	17.5	13.5	$^{12}\text{C}^+$, $^{18}\text{NH}_4^+$, $^{39}\text{K}^+$, $^{58}\text{C}_2\text{H}_5\text{NHCH}_2^+$, $^{97}\text{HSO}_4^-$, $^{195}\text{H}(\text{HSO}_4)_2^-$
EC-aged	53337	10.9	10.0	17.2	C_n^\pm ($n=1\sim 5$), $^{39}\text{K}^+$, $^{97}\text{HSO}_4^-$
Dust	52533	10.7	20.3	1.3	$^{40}\text{Ca}^+$, $^{56}\text{CaO}^+$, $^{16}\text{O}^-$, $^{17}\text{OH}^-$, $^{76}\text{SiO}_3^-$, $^{79}\text{PO}_3^-$
NaK-SN	13726	2.8	na	na	$^{23}\text{Na}^+$, $^{39}\text{K}^+$, $^{62}\text{NO}_3^-$, $^{97}\text{HSO}_4^-$
Metal	4672	1.0	na	na	$^{51}\text{V}^+$, $^{56}\text{Fe}^+$, $^{64,66,68}\text{Zn}^+$, $^{206,207,208}\text{Pb}^+$
Others	1580	0.3	na	na	No obvious characteristic peaks

833

834 **Figure captions:**

835 **Figure 1.** Box and whisker diurnal plots of the number concentration of the main particle
836 types (a) rich-Potassium (K), (b) Biomass burning (BB), (c) Organic carbon (OC), (d)
837 Ammonium, (e) Element carbon (EC)-aged, (f) Dust in hourly resolution. The lower, middle,
838 and upper lines of the boxes denote the 25th, 50th, and 75th percentiles. The lower and upper
839 whiskers show the 10th and 90th percentiles, respectively. Average values are shown in white
840 dots.

841 **Figure 2.** Maps of the mean HYSPLIT back trajectory clusters (72 h) at the height of 500 m
842 during the whole field observation. [Embedded pie chart represents the relative fraction of](#)
843 [each particle type in the four clusters.](#)

844 **Figure 3.** Size distributions of (a) the total number particle counts, (b) the relative
845 percentages (%) of the total particles for nine groups during the sampling campaign.

846 **Figure 4.** Number fractions of secondary markers associated with the six particle types
847 (rich-K, BB, OC, Ammonium, EC-aged, Dust). Secondary species include sulfate ($^{97}\text{HSO}_4^-$),
848 sulfuric acid ($^{195}\text{H}(\text{HSO}_4)_2^-$), nitrate ($^{62}\text{NO}_3^-$), ammonium ($^{18}\text{NH}_4^+$), amine ($^{58}\text{C}_2\text{H}_5\text{NHCH}_2^+$),
849 and oxalate ($^{89}\text{HC}_2\text{O}_4^-$) ions.

850 **Figure 5.** [Number fractions of secondary markers associated with the six particle types \(i.e.,](#)
851 [rich-K, BB, OC, Ammonium, EC-aged, and Dust\) in four clusters. Secondary markers](#)
852 [include sulfate \(\$^{97}\text{HSO}_4^-\$ \), sulfuric acid \(\$^{195}\text{H}\(\text{HSO}_4\)_2^-\$ \), nitrate \(\$^{62}\text{NO}_3^-\$ \), ammonium \(\$^{18}\text{NH}_4^+\$ \),](#)
853 [amine \(\$^{58}\text{C}_2\text{H}_5\text{NHCH}_2^+\$ \), and oxalate \(\$^{89}\text{HC}_2\text{O}_4^-\$ \).](#)

854 **Figure 6.** Correlations between the relative number fractions of the secondary species (a)
855 $^{43}\text{C}_2\text{H}_3\text{O}^+$, (b) $^{89}\text{HC}_2\text{O}_4^-$, (c) $^{18}\text{NH}_4^+$, (d) $^{62}\text{NO}_3^-$, (e) $^{97}\text{HSO}_4^-$ and O_x concentration during E1
856 (blue square) and E2 (red dot).

857 **Figure 7.** Correlations between the relative number fractions of the secondary species (a)
858 $^{43}\text{C}_2\text{H}_3\text{O}^+$, (b) $^{89}\text{HC}_2\text{O}_4^-$, (c) $^{18}\text{NH}_4^+$, (d) $^{62}\text{NO}_3^-$, (e) $^{97}\text{HSO}_4^-$ and relative humidity (RH)
859 during E1 (cyan dot) and E2 (orange square).

删除[Li]: ;

删除[Li]: the table embedded in the figure is the number concentration and relative fraction of the main six particle types in each cluster

删除[Li]: DEA (diethyl

删除[Li]: ;

删除[Online_Group]: S

设置格式[Li]: 字体: 小四, 字体颜色: 自动设置

删除[Li]: .

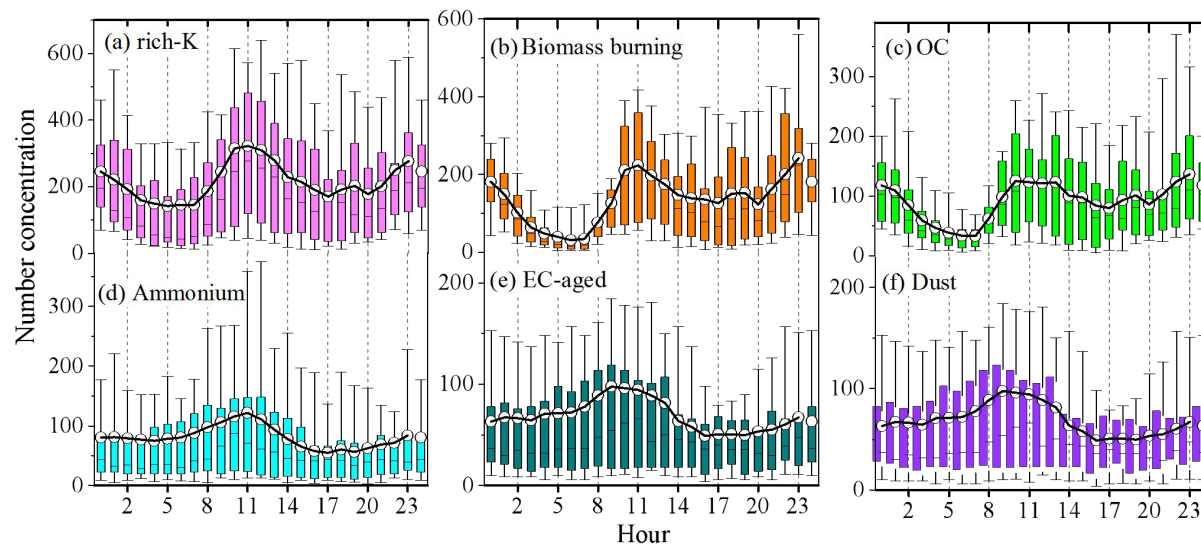
删除[Online_Group]: size distributions of the (a, c) number concentrations and (b, d) fractions of the major six particle types (rich-K, BB, OC, Ammonium, EC-aged, Dust) during two episodes of (a, b) E1 and (c, d) E2

设置格式[Li]: 字体颜色: 自动设置

删除[Online_Group]: **Figure 6.** Number fractions of secondary markers associated with the six particle types (rich-K, BB, OC, Ammonium, EC-aged, Dust) in two episodes events of E1 and E2: sulfate ($^{97}\text{HSO}_4^-$), sulfuric acid ($^{195}\text{H}(\text{HSO}_4)_2^-$), nitrate ($^{62}\text{NO}_3^-$), ammonium ($^{18}\text{NH}_4^+$), amine (DEA (diethylamine, $^{58}\text{C}_2\text{H}_5\text{NHCH}_2^+$), and oxalate ($^{89}\text{HC}_2\text{O}_4^-$).

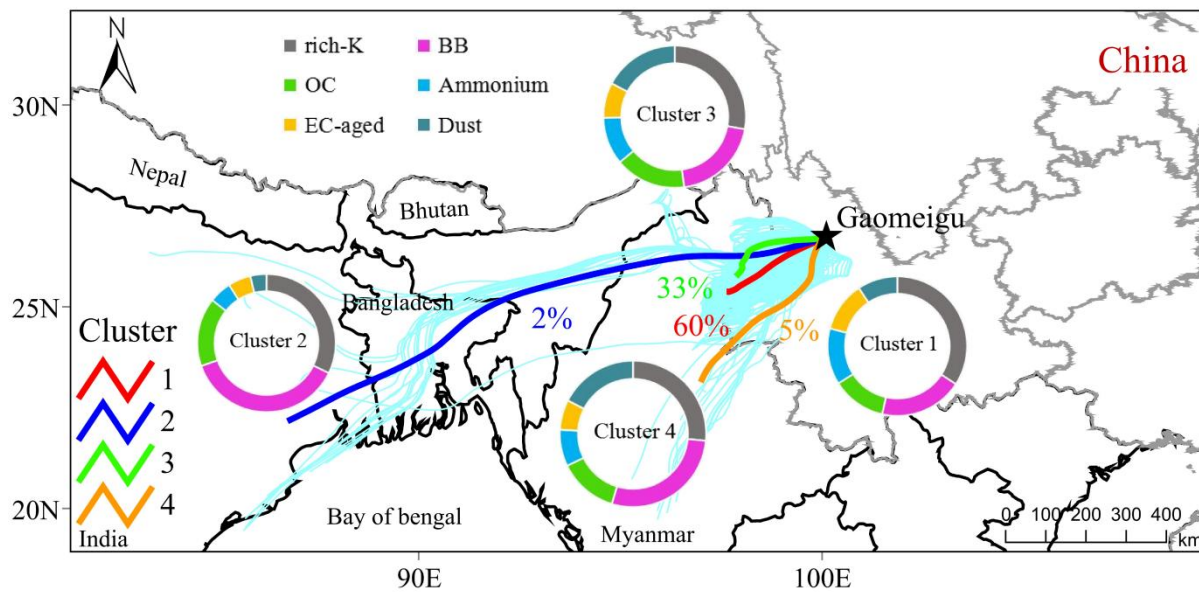
删除[Online_Group]: 7

删除[Online_Group]: 8



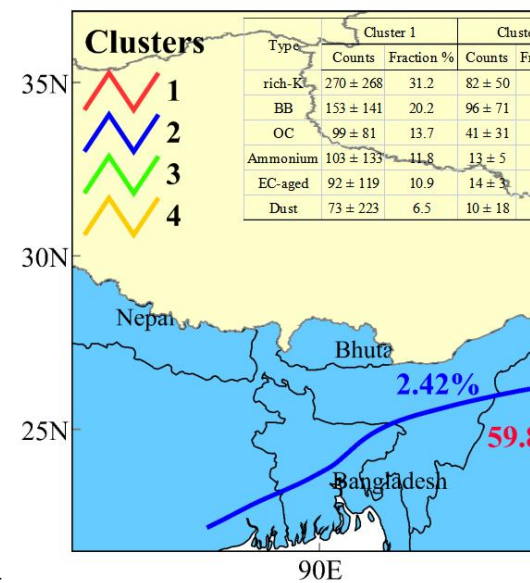
860

861 Figure 1. Box and whisker diurnal plots of the number concentration of the main particle types (a)
 862 rich-Potassium (K), (b) Biomass burning (BB), (c) Organic carbon (OC), (d) Ammonium, (e) Element
 863 carbon (EC)-aged, (f) Dust in hourly resolution. The lower, middle, and upper lines of the boxes denote the
 864 25th, 50th, and 75th percentiles. The lower and upper whiskers show the 10th and 90th percentiles,
 865 respectively. Average values are shown in white dots.

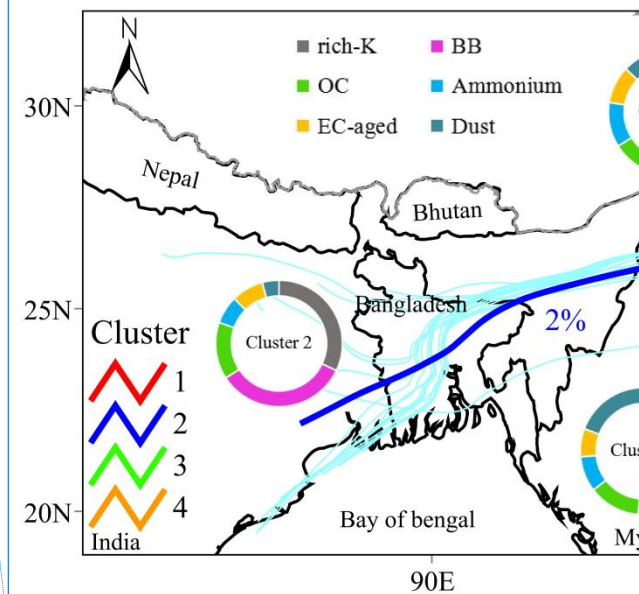


866

867 Figure 2. Maps of the mean HYSPLIT back trajectory clusters (72 h) at the height of 500 m during the
 868 whole field observation. Embedded pie chart represents the relative fraction of each particle type in the
 869 four clusters.



删除[Li]:



删除[Li]: ;

删除[Li]: the table e

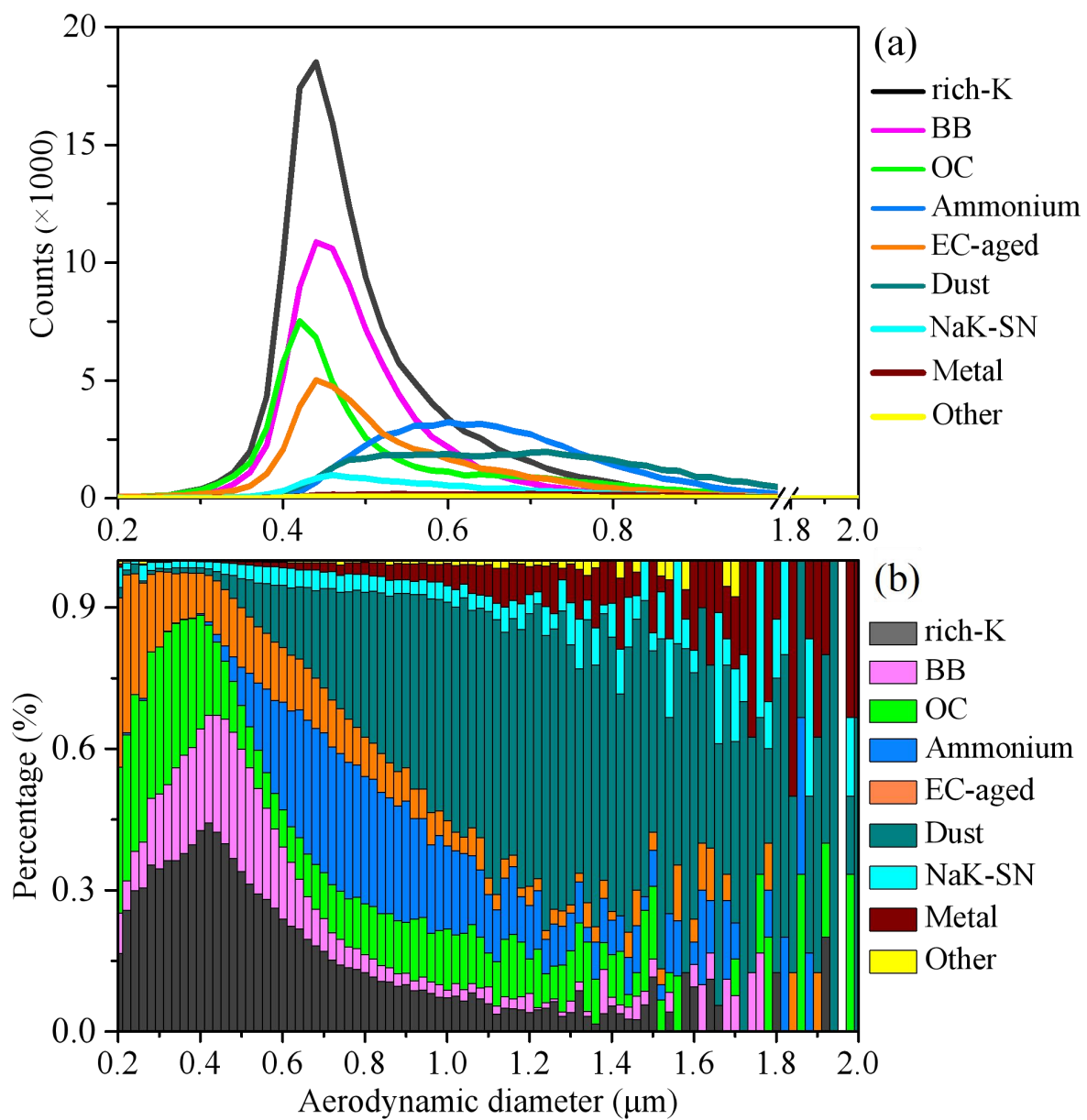
删除[Li]: in the figure is

删除[Li]: number concentration and

删除[Li]: the main six

删除[Li]: s

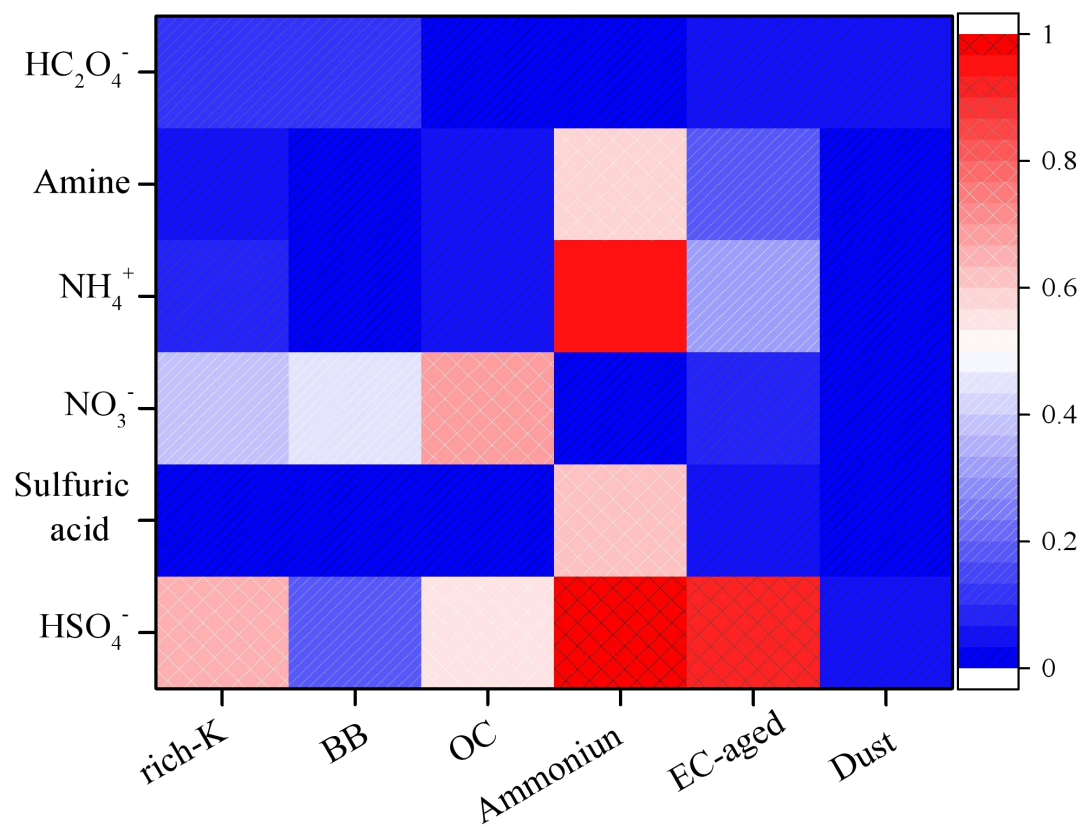
删除[Li]: each



870

871 Figure 3. Size distributions of (a) the total number particle counts, (b) the relative percentages (%) of the

872 total particles for nine groups during the sampling campaign.

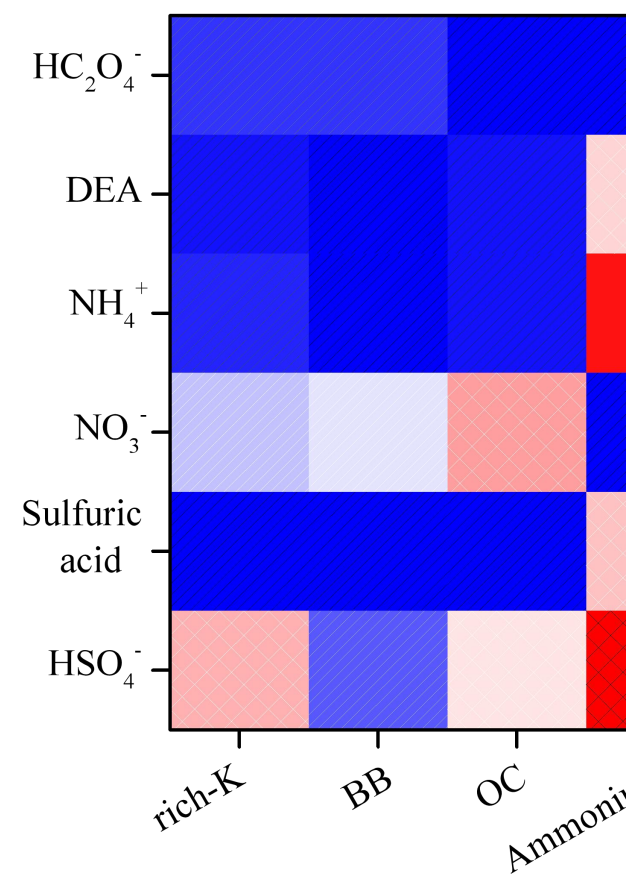


873

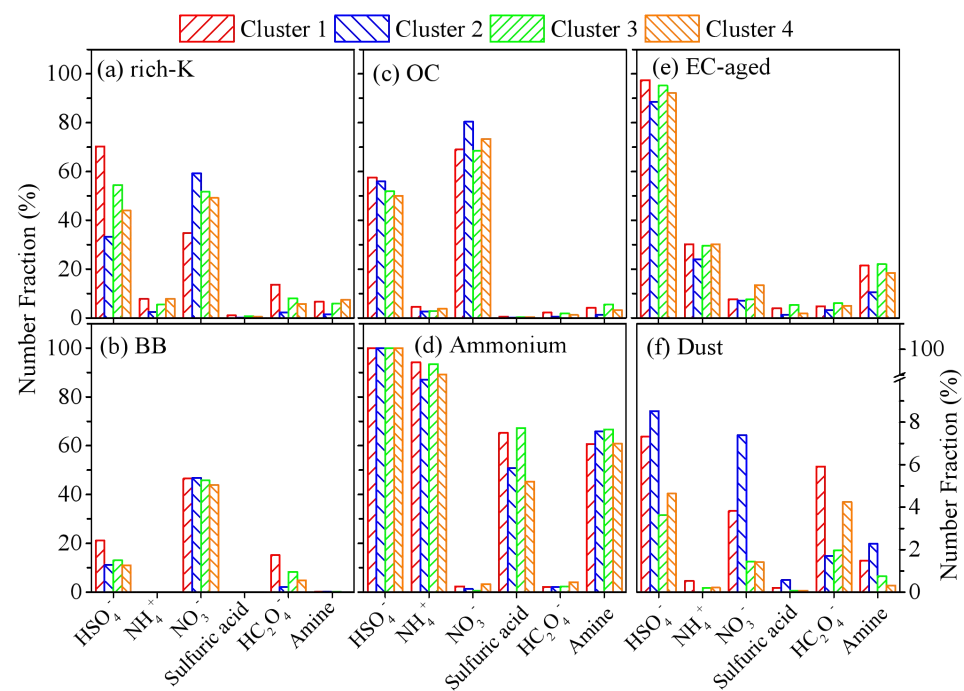
874 Figure 4. Number fractions of secondary markers associated with the six particle types (rich-K, BB, OC,
 875 Ammonium, EC-aged, Dust). Secondary species include sulfate (⁹⁷HSO₄⁻), sulfuric acid (¹⁹⁵H(HSO₄)₂⁻),
 876 nitrate (⁶²NO₃⁻), ammonium (¹⁸NH₄⁺), [amine](#) (⁵⁸C₂H₅NHCH₂⁺), and oxalate (⁸⁹HC₂O₄⁻) ions.

877

删除[Li]:



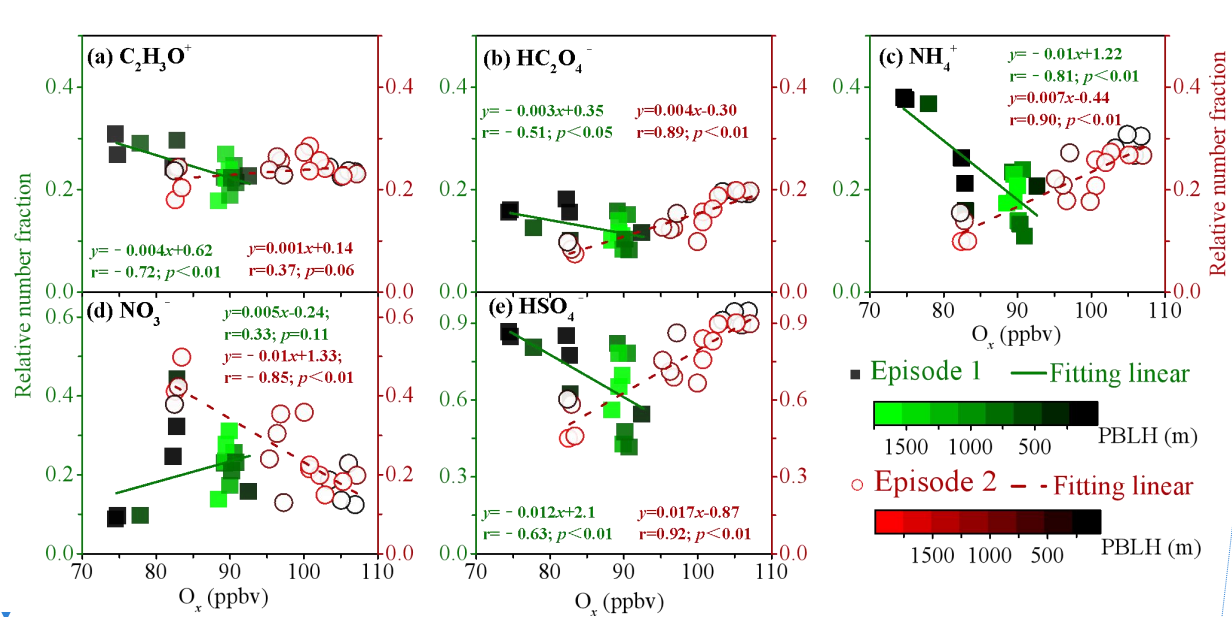
删除[Li]: DEA (diethylamine,



878

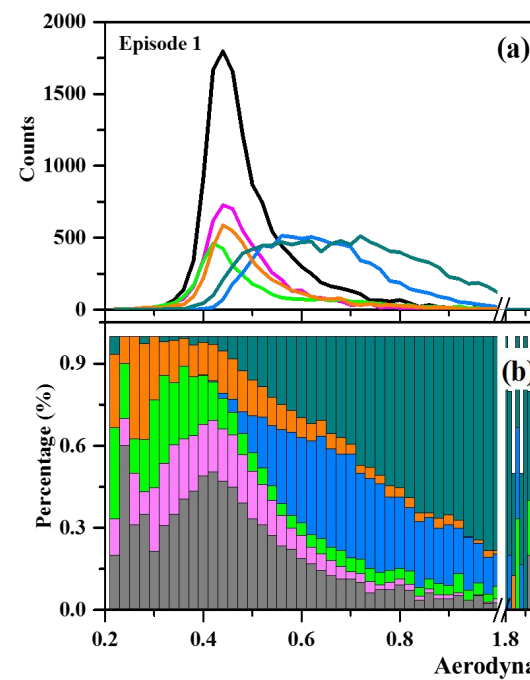
879 Figure 5. Number fractions of secondary markers associated with the six particle types (i.e., rich-K, BB,
 880 OC, Ammonium, EC-aged, and Dust) in four clusters. Secondary markers include sulfate (⁹⁷HSO₄⁻),
 881 sulfuric acid (¹⁹⁵H(HSO₄)₂⁻), nitrate (⁶²NO₃⁻), ammonium (¹⁸NH₄⁺), amine (⁵⁸C₂H₅NHCH₂⁺), and oxalate
 882 (⁸⁹HC₂O₄⁻).

883



884

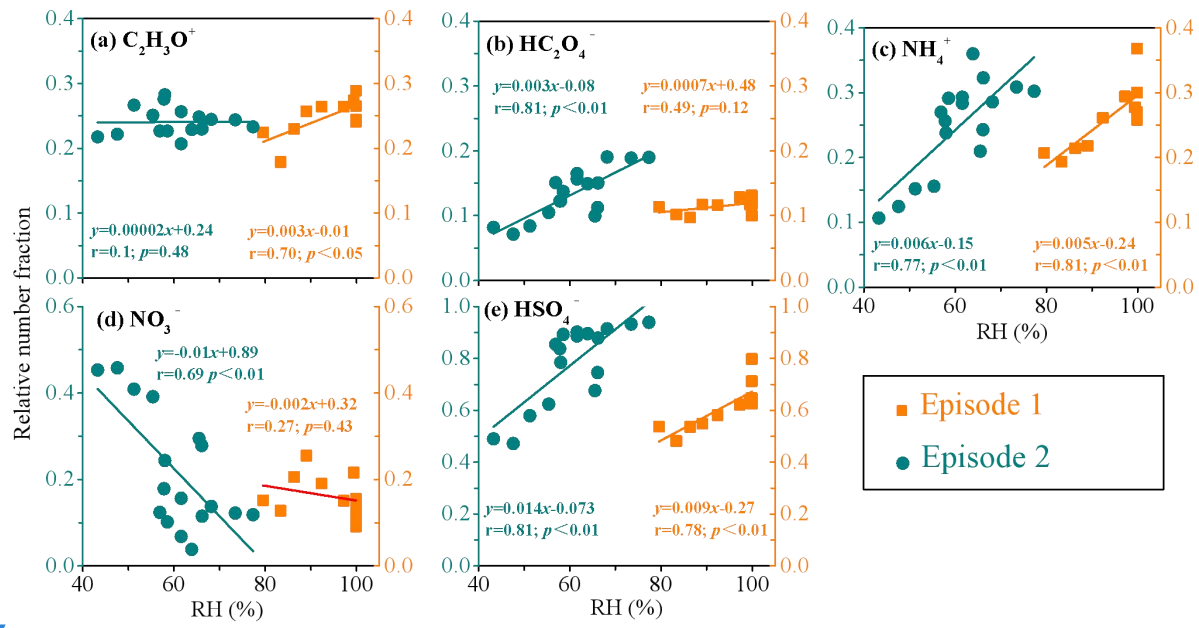
885 Figure 6. Correlations between the relative number fractions of the secondary species (a) $^{43}C_2H_3O^+$, (b)
 886 $^{89}HC_2O_4^-$, (c) $^{18}NH_4^+$, (d) $^{62}NO_3^-$, (e) $^{97}HSO_4^-$ and O_x concentration during E1 (blue square) and E2 (red
 887 dot).



删除[Li]:

Figure 5. Size distributions of the (a, c) number concentrations and (b, d) fractions of the major six particle types (rich-K, BB, OC, Ammonium, EC-aged, Dust) during two episodes of (a,b) E1 and (c, d) E2.

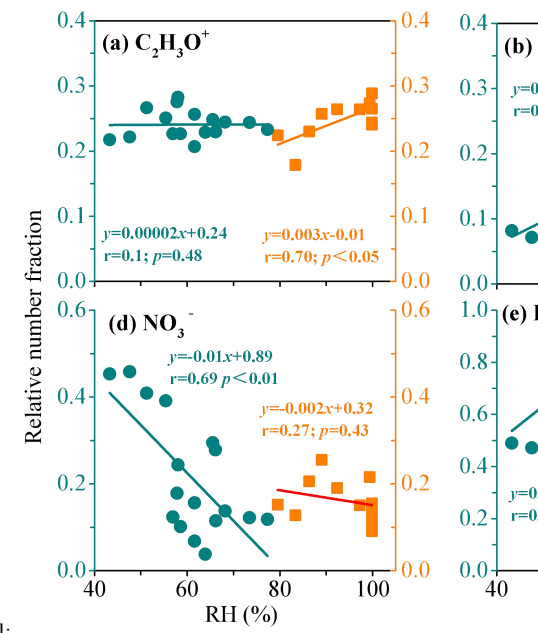
删除[Online_Group]: 7



888

889 Figure 7. Correlations between the relative number fractions of the secondary species (a) $^{43}C_2H_3O^+$, (b)
 890 $^{89}HC_2O_4^-$, (c) $^{18}NH_4^+$, (d) $^{62}NO_3^-$, (e) $^{97}HSO_4^-$ and relative humidity (RH) during E1 (cyan dot) and E2
 891 (orange square).

892



删除[Li]:

删除[Online_Group]: 8